Journal of the Brazilian Society of Mechanical Sciences and Engineering (2023) 45:275
https://doi.org/10.1007/s40430-023-04178-x

TECHNICAL PAPER

Energy absorption of the additively manufactured novel re-entrant auxetic structure in comparison with honeycomb structure: experimental and numerical analysis

Mohsen Safikhani Nasim[1] · **Amin Yaghootian**[1] · **Reza Mosalmani**[1]

Received: 18 November 2022 / Accepted: 27 March 2023 / Published online: 28 April 2023

Abstract

The energy absorption and negative Poisson's ratio (NPR) of a novel re-entrant auxetic structure were examined under quasi-static compression loading in this study, along with their comparison to a non-auxetic honeycomb utilizing experimental study and numerical analysis. The specimens were made using additive manufacturing (3D printing). The results show that auxetic structures' energy absorbed at least 57.75% better than non-auxetic honeycombs. In addition, NPR behavior and energy absorption are affected by the geometrical characteristics of the unit cell as well as the material of the re-entrant auxetic structure. According to the results, the Poisson's ratio got more negative, and the auxetic property increased when the oblique length and initial characteristic angle were raised. In contrast with these two characteristics, Poisson's ratio rises as structure thickness increases while the auxetic property decreases.

Technical Editor: Samikkannu Raja.

✉ Amin Yaghootian
a.yaghootian@scu.ac.ir

[1] Mechanical Engineering Department, Faculty of Engineering, Shahid Chamran University of Ahvaz, Ahvaz, Iran

Graphical abstract

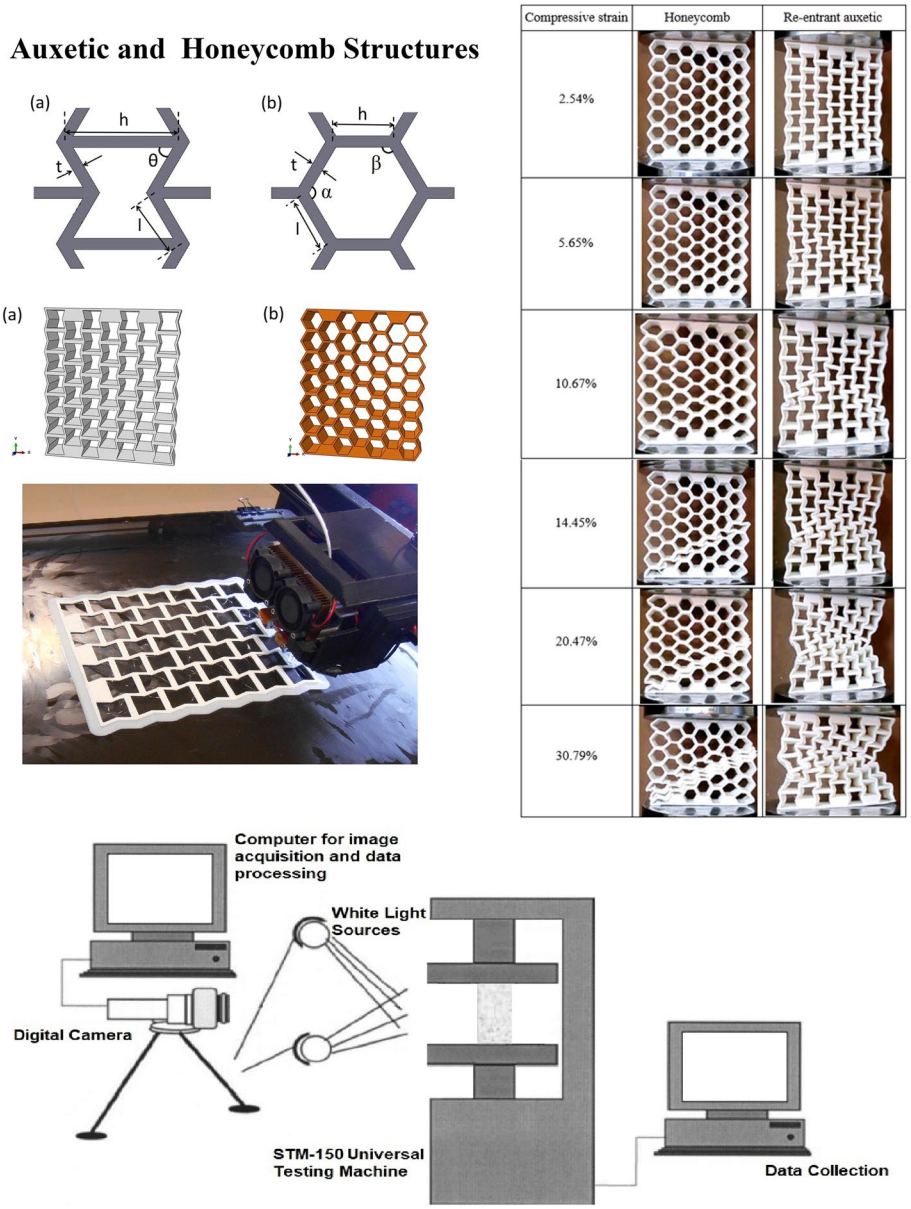

Keywords Negative Poisson's ratio · Auxetic structures · Energy absorption · Quasi-static loading · Specific energy absorbed · Honeycomb structure

1 Introduction

The Poisson's ratio of auxetic materials is negative (NPR). As a result, these materials expand in the transverse direction when stretched in one direction while shrinking in width when compressed [1]. Auxetic materials also absorb a lot of impact energy [2]. These materials also have high shear strength [3], surface descending resistance [4], fracture toughness [5], and a high acoustic energy absorption rate [6]. A variety of industries have used these materials, including the automobile industry [7], aerospace and military [8–10], sensors [11], tissue science [12], and sports engineering [13, 14] due to their unique mechanical properties.

Lili et al. studied the behavior of composites constructed from polyurethane foam, ABS plastic tubes, and polyester fibers under quasi-static loading [15] and low-velocity impact[16].

Safikhani and Etemadi [17] studied the mechanical behavior of this sort of auxetic composite under quasi-static loading and methods for achieving a higher negative Poisson's ratio using the FEM. It was deduced from their stress–strain curves that this kind of composite material has a damping property. A decrease in the distance between ABS plastic tubes and an increase in foam density will result in a decrease in Poisson's ratio. Additionally, they have proposed a new auxetic structure in another paper [18] in which the unit cells are joined in a warp-and-woof pattern. Hou et al. [19] presented a composite structure with a negative Poisson's ratio. These composite structures were composed of re-entrant [20], chiral [21], star-shaped [22], and dual arrowhead [23] units. Various researches have been conducted on the static mechanical properties of auxetics. In two orthogonal directions, Wang et al. [24] evaluated the elastic characteristics of re-entrants by strain-based expansion homogenization.

A theoretical, numerical, and experimental study by Gao et al. [25] investigated double arrowhead structures intersected by honeycombs with negative Poisson's ratio. In the study, it was demonstrated that honeycomb crushing behaviors during large deformation differ from those under small deformation, including the mode of deformation, the mechanism of deformation, and the crushing strength [26]. Auxetic metallic honeycombs are used as cores in protective sandwich structures that are subject to large deformation [27]. Anti-trichiral honeycombs with large deformations were examined by Hu et al. [28]. Qi et al. [29] used the FEM to investigate sandwich structures with an auxetic core in a high-speed impact test and discovered that the structural efficiency increased from 150 to 350 m/s. Using molecular dynamics, Grujicic et al. [30] investigated the ballistic impact behavior of the Zeolite auxetic structure and found that maximum pressure and acceleration were decreased in this structure. Xin-tao et al. [31] created 3D cell designs that can absorb more energy. Simon et al. [32] developed energy-absorbing flexible cellular structures. Yaun [33] created several three-dimensional structures utilizing selective laser sintering with auxetic properties. Evans [34] designed a sandwich panel with a reticular core and a re-entrant auxetic geometrical shape. Yang et al. [35] investigated the effect of variations in cell thickness of auxetic structures on energy absorption under dynamic and static loading to incorporate them into body protection blocks. Hamzei et al. [36] developed a novel octagonal model with auxetic properties during compressive deformations. Zhang et al. [37] investigated the dynamic destructive impacts of various auxetic internal plate structure degrees. Ingrol et al. [38] demonstrated that there is a significant relationship between the geometrical specification of structures, the structure of their cells, and the macromechanical and micromechanical properties of the auxetic mesh structure by modifying the re-entrant structure and comparing it to the initial structure in energy absorption. Due to the difficulties and complexities associated with fabricating auxetic structures with a variety of shapes, additive manufacturing (3D printing) is an appropriate solution [39].

Wanli Xu et al. [40] studied the energy absorption rate of auxetic warp-knitted spacer fabric composite under low-velocity impact. Chang Qi et al. [41] designed a novel type of auxetic cells and then experimentally and statistically assessed the behavior of NPR under quasi-static loading. Meena and Singamneni[42] presented the S-shape structure as an auxetic structure and compared the mechanical behavior of the new structure with that of the re-entrant structure. In this auxetic structure, the maximum Poisson's ratio is greater than in a re-entrant structure. Min Hur et al. [43] developed tubular structures using auxetic patterns and discovered that their mechanical properties were improved when compared to similar structures. Mizzi et al. [44] developed and studied auxetic plates subjected to tensile forces. Linforth et al. [45] built several auxetic oval structures and evaluated their energy absorption rate under quasi-static and dynamic loading conditions.

Ajdari et al. [46] studied hierarchical honeycombs' mechanical properties and behavior. By converting the foam cell structure into re-entrant, Choi and Lakes[47] concluded that Young's modulus of the foam decreased with a permanent volumetric compression ratio.

An analysis of the elastic properties of honeycomb structures with negative Poisson's ratios by Zhang et al. [48] revealed that geometric parameters greatly affected elastic modulus. By designing the geometric parameters of the honeycomb, its mechanical performance can be optimized for specific applications. Imbalzano et al.[49], blast resistance of structures, examined the auxetic and honeycomb sandwich panels. It concluded that the re-entrant structure was more resistant to the impact of the blast due to its negative Poisson ratio.

The findings of the past studies indicated that the computation of mechanical properties of auxetic structures has always been considered. A parametric auxetic structure is first designed and produced using additive manufacturing (3D printing) in this research. The purpose of this study is to investigate both experimentally and numerically the behavior of re-entrant auxetic structures under quasi-static compression loading. Furthermore, the re-entrant auxetic structures are compared with honeycomb structures, which are commonly used as energy absorbers. Additionally, experimental testing and finite element simulation are used to analyze the mechanical behaviors of the structure, as well as the parameters affecting energy absorption and NPR behavior, such as initial angle, wall thickness, length of horizontal and oblique members, and structure material; also, Sect. 2 describes how experiments were conducted on the built auxetic structure. Section 3 describes the finite

element simulation method, and Sect. 4 reviews and discusses the results.

2 Experiments

In this study, two structures are examined, one which is a re-entrant auxetic structure and the other which is a non-auxetic honeycomb structure. Figure 1-a presents the 2D view of the constitutive cellular auxetic structure, in which $l = 12.375$ mm, $h = 25.51$ mm, $\theta = 75°$, and $t = 2.25$ mm. Figure 1b presents a 2D view of the honeycomb structure, in which $h = l = 13.01$ mm, $\alpha = \beta = 120°$, and $t = 2.25$ mm. The cell numbers and general dimensions of models, such as length, width, height, and weight, were chosen to be the same to compare these structures. Two different models were prepared in $168.61 \times 183.63 \times 40$ mm^3. Figure 2 illustrates the design of the auxetic structures and honeycomb structures used in this study. These designs were used to be made through the 3D printing process.

Poisson's ratio, which is related to their cell units, differentiates re-entrant structures from honeycomb structures. As honeycomb cells have a positive Poisson's ratio when stretched in one direction, they contract in the transverse direction, and when loaded in compression, they expand. On the other hand, the re-entrant cells have a negative Poisson's ratio, and when they are stretched in one direction, they expand in the transverse direction to the loading direction. Thus, the cells contract in the transverse direction if the load is reversed from tension to compression.

Three samples of each structure were made by additive manufacturing. The printer used was the Author M Pro, and the material was polylactic acid (PLA) from the Yousu Company. There exist several methods and techniques that can be employed to assess the internal and external condition of these components, including non-destructive testing (NDT). NDT of 3D-printed parts is among the recent research areas presently under development. In this study, the manufacturing process of 3D printing was meticulously carried out to ensure the production of defect-free and high-quality printed parts. Then, the manufactured samples were then checked for their thickness and geometric dimensions. The samples were consistent with the designed parts, had smooth surfaces, and were free of geometric defects. Furthermore, the manufacturing conditions were maintained identically for all the samples. Further to the lattice structures, specimens made according to ASTM D638 were tested under tensile loading to determine the mechanical properties of the material. Tensile specimens have been made using the same 3D printing process and specifications. Figure 3 shows the geometry and a 3D-printed sample. Material properties of PLA are listed in Table 1, and Fig. 4 shows the PLA stress–strain diagram.

Using a universal testing machine (STM-150) from Santam, compression tests were conducted on auxetic and honeycomb structures according to ASTM D1621 standards. Figure 5 shows a schematic diagram of the quasi-static compression test setup. Figure 6 shows the 3D re-entrant auxetics structure under quasi-static loading. In this experiment, the loading speed was set at 2 mm/min, and the temperature was $25^{\circ} \pm 3^{\circ}$C.

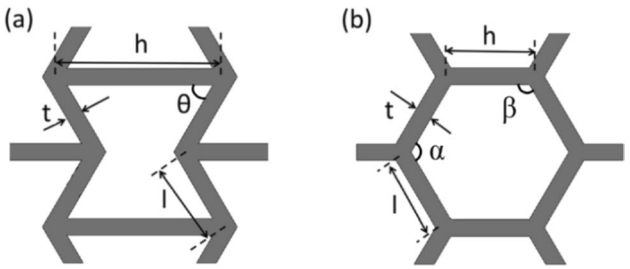

Fig. 1 Designs for single cell: **a** re-entrant auxetic and **b** honeycomb

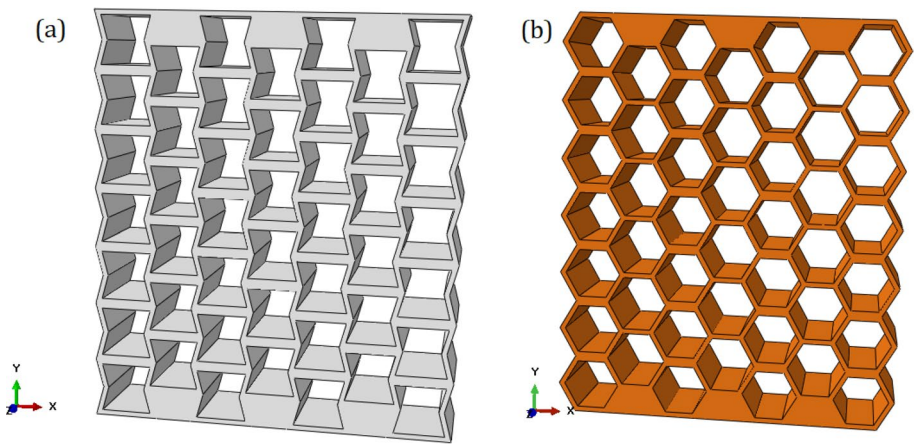

Fig. 2 Structures created by cells: **a** re-entrant auxetic and **b** honeycomb

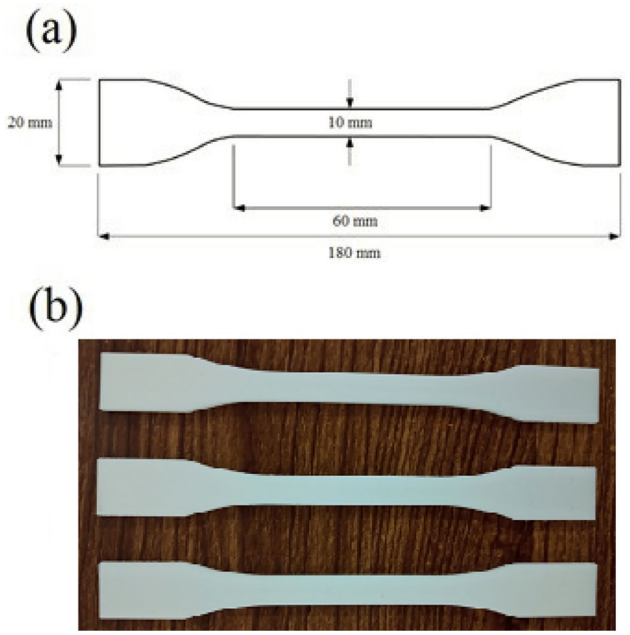

Fig. 3 Test of uniaxial tensile strength of PLA: **a** specimen geometry and **b** specimens 3D printed

Table 1 PLA, steel 4340, aluminum 1100, and OFHC copper mechanical properties[50–54]

Sample	Young's modulus (E) GPA	Poisson's ration	Density (ρ)g/cm^3
PLA	1.57	0.36	1.24
Steel 4340	200	0.29	7.83
Aluminum 1100	69	0.27	2.71
OFHC copper	129.8	0.34	8.96

While doing the compression test, the vertical displacement of the sample was recorded directly by the testing machine, and a camera was set up at 50 cm in front of the model to record the width variations of the sample. For each second, three shots were taken to measure the transverse displacement and study the angles of structures. The displacements of each point and angle change of structures were manually analyzed by the Digimizer Image Analysis Software [55] and the DIC method in MATLAB. Calculating the changes in angles α, β, and θ during compression involves measuring the angle at each compression stage using Digimizer software and comparing it with the angle of the cell before compression. The Poisson's ratio of the tested model is obtained using measured axial strain ($\varepsilon_{\text{axial}}$) and transverse strain ($\varepsilon_{\text{trans}}$) as follows:

$$\nu = -\frac{\varepsilon_{trans}}{\varepsilon_{\text{axial}}} \tag{1}$$

3 Finite element simulation

3.1 FE simulation of the auxetic structure

The finite element analysis with ABAQUS software was used to study the auxetic structure. In order to mesh the sample, HyperMesh software was used due to the complexity of the structure and the limitations of ABAQUS. The material type is considered an elastic–plastic material. In addition, the effects of temperature and strain rate on mechanical properties are neglected. Figure 7a shows the meshing of the auxetic structure. The meshing of the models was performed using linear 8-node C3D8R elements, and the mesh was sweep with hexahedral elements. Boundary conditions and loading are the same as in Sect. 2. The boundary condition in the software is also the same as in Fig. 7b, which is applied to all models. The models are located between two rigid plates. With a friction coefficient of 0.20, interaction features are defined by a contact constraint. The rigid bottom plate is fixed completely, and the rigid top plate's movement is only allowed to perform on *Y*-axis.

In order to achieve an optimal mesh, it is necessary to take into consideration the effects of mesh sensitivity on the results. Consequently, it is necessary to investigate the mesh's type, shape, and size. As shown in Fig. 8, the displacement of the structure is obtained by changing the element size. Results show that displacement does not change significantly for elements smaller than 4 mm. Therefore, a 4-mm element is selected, and the total number of elements is 76,960.

3.2 FE Simulation of quasi-static compression test

In quasi-static problems, the loading rate is very low. In quasi-static tests, the jaw movement speed of the device is considered to be 2 mm/min. The analysis time would be 9000 s for a change of shape equivalent to 300 mm if this speed was applied to the structure. This is both very large and practically impossible. For this reason, both mass effects and analysis time should be reduced in order to perform a low cost, accurate, and correct analysis. Different methods can be used separately or simultaneously to perform a quasi-static analysis. One of the test methods is applying load smoothly. In order to perform a quasi-static analysis, the applied force should be applied slowly to the structure. An example of a slowly applying load is shown in Fig. 9 [56].

As illustrated in Fig. 9, the initial speed and slope of the diagram (initial acceleration) are zero. This loading method eliminates undesired effects during quasi-static simulation. Following a quasi-static analysis, the simulation's correctness can be verified using two simple tests:

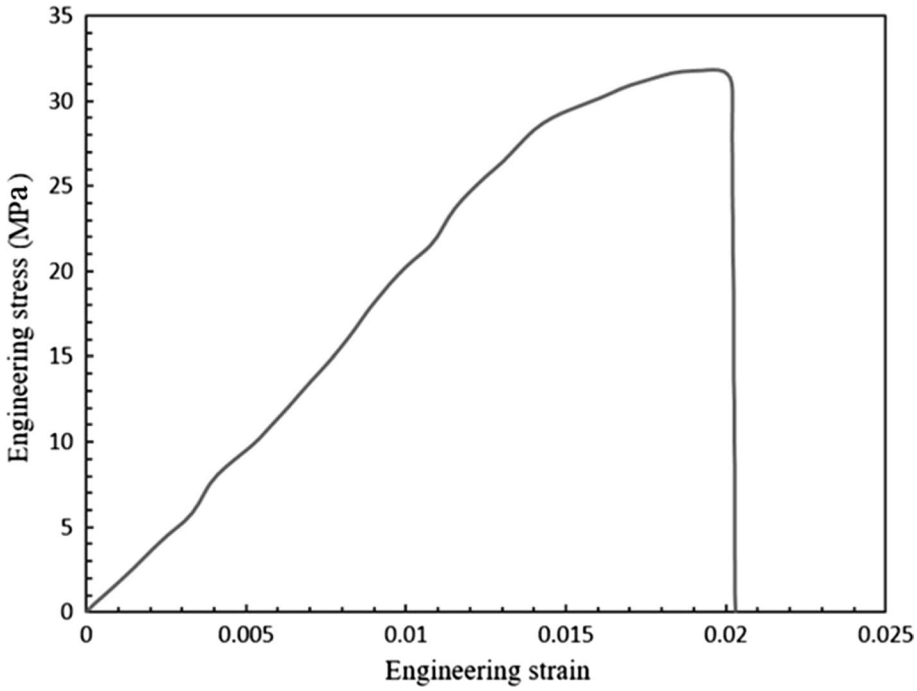

Fig. 4 Tensile stress–strain of PLA

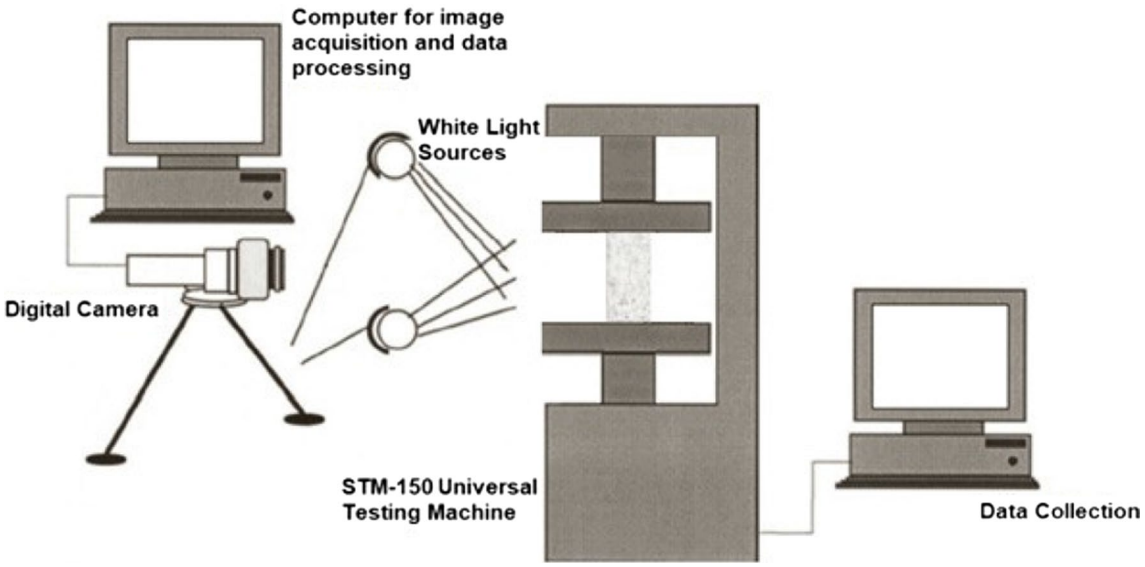

Fig. 5 Schematic diagram of the quasi-static compression test setup

1. A pseudo-static analysis will result in low ingredient velocity, which, in turn, will result in negligible mass forces. Thus, the internal force equals the outlet work performed, and kinematic energy is negligible in comparison with internal energy [57].
2. There is no variation in the force vs. displacement diagram at different speeds [57–59].
3. The method of slowly applying load is used in this article in order to simulate quasi-static pressure. Furthermore, internal and kinetic energy are evaluated to ensure quasi-static simulation performance. Figure 10 shows the relevant diagram. Considering that kinematic energy is negligible compared to internal energy, the analysis can be regarded as quasi-static.

Fig. 6 The re-entrant auxetics structure under quasi-static loading

4 Results and discussion

4.1 Comparison of honeycomb and re-entrant structures and validation of results

In order to compare the numerical and experimental results, tests were conducted according to each numerical model. The re-entrant auxetic and non-auxetic honeycomb samples were loaded up to 65.98% and 57.09% of their initial length, respectively. In these percentages of compression, the structure has collapsed, and the structure is condensed, resulting in an increase in stress levels. The surface under the stress–strain diagrams has been considered for calculating energy absorption and specific energy absorption up to the height reduction of 50% to equalize the comparison conditions between structures. In this article, the quasi-static compression was simulated by slowly applying compressive load. A comparison of the kinetic energy and internal energy of the specimen is presented in Fig. 10. Since the contribution of kinetic energy is negligible, it can be concluded that the velocity of the compression process was suitable; therefore, the process can be considered quasi-static.

In Fig. 11, non-auxetic honeycomb and re-entrant auxetic structure deformation are shown for strains 2.54%, 5.65%, 10.67%, 14.45%, 20.47%, and 30.79%.

Figures 12 and 13 show the comparison between the stress–strain diagrams of the numerical modeling and experiment of non-auxetic honeycomb and auxetic re-entrant structures, respectively. The cell walls bend when the honeycomb structure is compressed on its plane (x–y). This deformation is initially a linear elastic deformation. The cells, however, fall when the strain reaches a critical level due to elastic or plastic buckling. These collapses are related to constitutive material specification, as shown in Ref. [38]. If the walls of the unit cell collide because of the applied compression, the collapse will be completed, and the absorption of energy be highly reduced. Furthermore, if all the cells collapse due to more compression, material stiffness will increase, and the structure will be denser. Similar results have been shown by Gibson and Ashby [60] for an aluminum lattice structure.

When the walls of collapsed cells press against each other, the amount of load will rise significantly. The load amount is continuously increased and decreased until all structure cells are destroyed. From this point on, if the structure continues to be compressed, the load will rise significantly, showing that the structure is getting denser. According to Figs. 12 and 13, this process is the same for honeycomb and re-entrant structures.

There are three stages to this stress–strain curve, as illustrated in Figs. 12 and 13. Stress–strain curves are linear during the first stage. Then, by collapsing each cell, the force will decrease, and this decrease can be seen up to a 30% change in height. The second stage is related to when vertical walls are bent, and the structure shows auxetic properties. However, the vertical walls of the cells have not yet come together. As the walls come together and the middle rows are compressed, the amount of force increases slightly, which results in small peaks, as shown in the second stage. After the relative compaction of the middle rows of the structure, the structure's stiffness increases slightly. The stress level rises continuously until the whole structure collapses, moving toward condensation. The third stage of the diagram represents this part of the deformation.

The stability of force amounts after the first maximum point indicates that the structure has deformed uniformly and forces are distributed equally. In re-entrant and honeycomb structures, the concentration of the force happens in only one of the rows, which will cause significant diagram ascent and descent in the force diagram.

One of the main reasons for using lattice structures is their high-energy absorption capacity. By calculating the area under stress–strain curves using Eq. 4, one can obtain the amount of energy absorbed by a structure (W):

$$W = \int_0^{\varepsilon} \sigma(\epsilon)\, d\epsilon \tag{4}$$

For all samples, the amount of absorbed energy was calculated. However, it is pertinent to note that the total

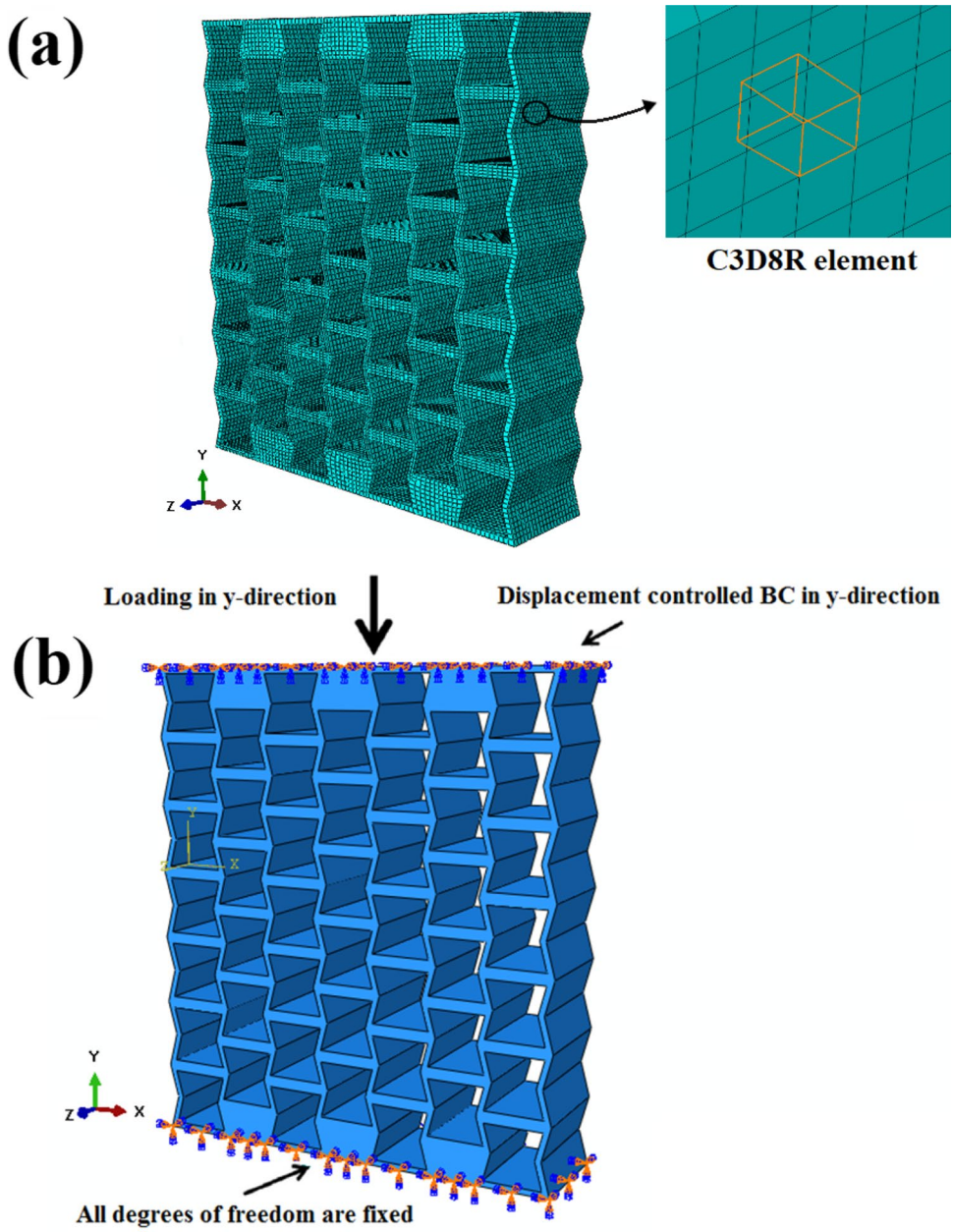

Fig. 7 FE simulation: **a** re-entrant auxetic structure including sweep mesh with hexahedral elements and **b** appling boundary conditions and load in Abaqus software

energy absorbed by structures cannot be used alone as a criterion. In order to account for the structure's weight effects, a variable called "specific energy absorption" is defined. Specific energy absorption is calculated by dividing the structure's total energy absorption by its weight, using Eq. 5 [38].

$$W_s = \frac{\int_0^{\varepsilon} \sigma(\varepsilon) d\varepsilon}{\rho \Delta \rho} \tag{5}$$

where $\Delta\rho$ is the relative density, and according to auxetic re-entrant and non-auxetic honeycomb cells, Fig. 1-a and b is calculated, respectively, as [61]:

$$\Delta\rho = \frac{\rho^*}{\rho} = \frac{1}{2}\frac{t}{l}\frac{\left(\frac{h}{l}+2\right)}{\sin\theta\left(\frac{h}{l}+\cos\theta\right)} \tag{6}$$

$$\Delta\rho = \frac{\rho^*}{\rho} = \frac{1}{2}\frac{t}{l}\frac{\left(\frac{h}{l}+2\right)}{\sin\alpha\left(\frac{h}{l}-\cos\alpha\right)} \tag{7}$$

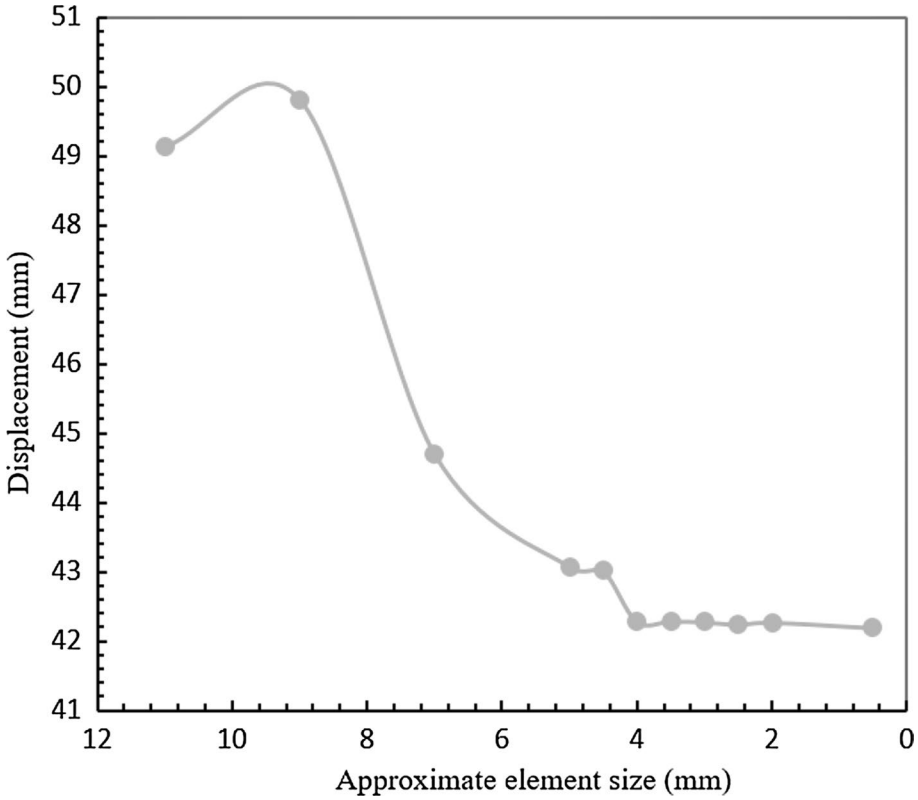

Fig. 8 Investigating the effect of the mesh size

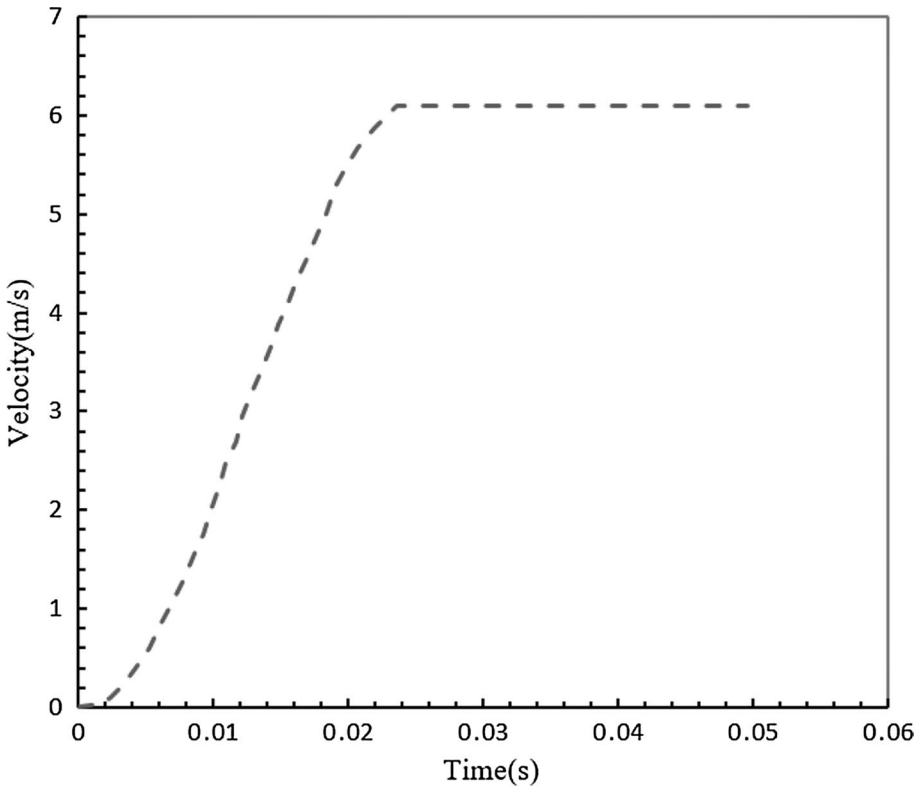

Fig. 9 Load history diagram used in quasi-static simulations[56]

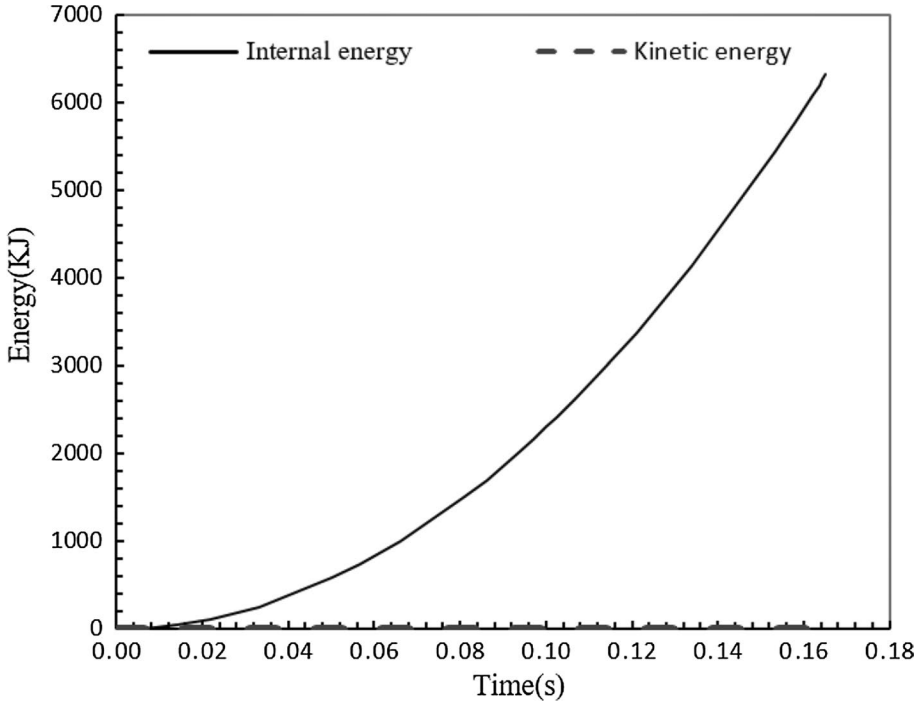

Fig. 10 History of kinetic energy and internal energy under quasi-static loading

The parameters h and l and angles $\theta and \alpha$ are defined in Fig. 1-a and b.

In order to equalize the comparison conditions between the structures, an area under each diagram up to a reduction in the height of approximately 50% was considered when calculating the energy absorption. Figures 14 and 15 show energy absorption and specific absorption energy, respectively. As can be seen, the absorption of the re-entrant auxetic structure is 7015.353 J/m^3. In comparison, the absorption of the non-auxetic honeycomb structure is 4446.890 J/m^3. Besides, the specific energy absorption rate of the re-entrant auxetic structure is 23.621 J/kg, and the specific energy absorption rate of the non-auxetic honeycomb structure is 18.718 J/kg. Therefore, the amount of energy absorption and specific energy of the auxetic re-entrant structure is 57.75% and 26.19%, respectively, more than the non-auxetic honeycomb structure. This result shows the excellent efficiency of auxetic structures in energy absorption. The behavior of the structures and the ability of high-energy absorption in a large deformation make the structures suitable for a wide range of applications, including crash absorbers, aerospace and defense applications, as well as protective equipment for sports. Furthermore, as shown in Figs. 12, 13, 14, and 15, experimental and numerical results are in excellent agreement. The difference is less than 6%.

The negative Poisson's ratio is calculated by Eq. 1. In Fig. 16, the experimental and numerical results are shown for the negative Poisson's ratio of re-entrant auxetic in different compression levels. The maximum values of the negative Poisson's ratio obtained from the experiment and FEM are presented in Table 2. In Table 2, the maximum relative error between experimental and numerical values for the negative Poisson's ratio is 3.78%.

The compressive strain in Fig. 16 can be divided into three regions based on the change in Poisson's ratio. With an increase in the strain from 0% to 2.54% in region I, the negative Poisson's ratio (in terms of absolute value) increases significantly from 0 to − 1.835 and reaches its maximum value of − 1.835. The situation occurs due to quasi-static loading and uniform deformation of auxetic cells in the elastic region (see Fig. 11 for re-entrant auxetic structures in strain 2.54%).

There is a linear decrease in NPR for strains from 2.54 to 10.67% in region II (from − 1.835 to − 0.988). The cause of this situation is plastic deformation in auxetic cells (see Fig. 11 for re-entrant auxetic structures in strains 5.65% and 10.67%).

In region III, initially due to the simultaneous collapse of several cells, NPR is temporarily prevented by increasing the strain upper than 10.67%. At strains higher than 14.45%, the structure reaches its maximum compaction. The walls of auxetic cells interfere with each other and reduce the effect of NPR. Therefore, the structure loses its auxetic behavior (see Fig. 11 for re-entrant auxetic structures in strains higher than 14.45%).

Figure 17 shows the NPR of the re-entrant structure with decreasing angle θ for a strain of 0–36.11%. As can be seen, with decreasing θ, the NPR of the structure increases until it reaches its maximum value of -1.835 at an angle of

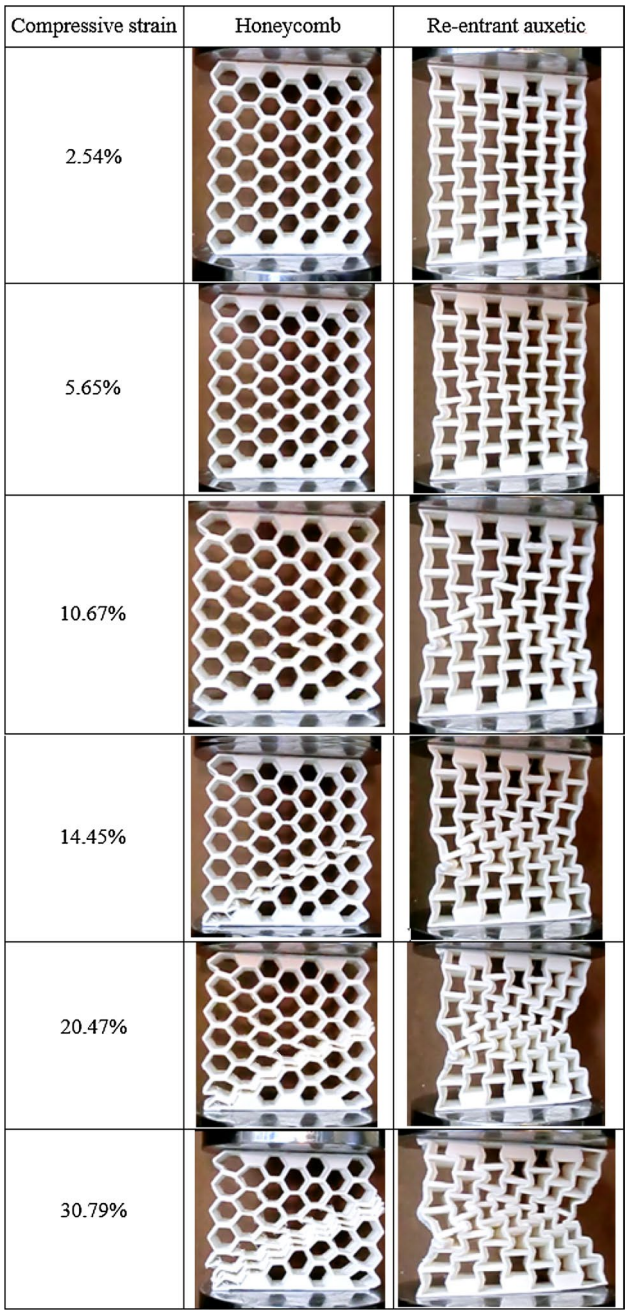

Fig. 11 The deformation of non-auxetic honeycomb and re-entrant auxetic for strains 2.54%, 5.65%, 10.67%, 14.45%, 20.47%, and 30.79%

$\theta = 65.95°$, and then, the NPR decreases due to the entanglement of the structure.

Figure 18 illustrates the comparison of Poisson's ratio of the honeycomb structure versus compressive strain based on experimental and numerical results. According to Fig. 18, the honeycomb structure exhibits a positive Poisson's ratio when subjected to quasi-static loading. Table 3 presents the maximum relative error of the positive Poisson's ratio between experiments and FEM. The relative error is 3.19%, which indicates good agreement.

Figures 19 and 20 show Poisson's ratio of honeycomb structure versus variation of angle α and angle β related to strain ranging from 0 to 10.18%, respectively. As it can be observed, with a decrease in angle α and an increase in the angle β, Poisson's ratio of the honeycomb structure increases, and at $\alpha = 90°$ and $\beta = 135°$ reach its maximum amount, which is 0.734. Afterward, Poisson's ratio of the structure decreases in strains higher than 10.18% according to the plastic deformation of the structure.

4.2 Investigation of the effect of the structure's material

Figure 21 presents the NPR variations determined by the finite element method for auxetic re-entrant structures of steel 4340, OFHC copper, or aluminum 1100. In Table 1, these materials' mechanical properties are listed. Table 4 presents the maximum negative Poisson's ratio related to these materials. According to Fig. 21 and Table 4, the maximum negative Poisson's ratio of Al is greater than Cu, and Cu is greater than PLA.

Additionally, the maximum negative Poisson's ratio of PLA is higher than steel. The results show that the maximum negative Poisson's ratio varies by 10% for various materials. As a result, the structure's geometry is more important than the material in the maximum negative Poisson's ratio. Figure 22 illustrates the stress–strain diagrams for all four models. In Table 4, the amount of energy absorbed and the amount of energy absorbed per unit volume for each model. As a result, steel has the highest amount of energy absorbed and specific energy absorbed, and PLA has the lowest.

4.3 Investigating the effect of geometry

The constitutive cellular structure of an auxetic structure is shown in Fig. 1a. A variety of geometry size re-entrant auxetic structures is designed to better understand the effects of geometry size on the NPR behavior of auxetic structures. These structures are listed in Table 5. Simulating and analyzing them has been done using the finite element method.

In order to investigate the effect of wall thickness, stress–strain diagrams, and Poisson's ratio in terms of the compressive strain of structures, A_0,t_1 and t_2 are given in Figs. 23 and 24, respectively. In Fig. 24, the maximum value of the negative Poisson's ratio is for the structure A_0 with a value of − 1.835. The stress that is placed on the re-entrant auxetic structure increases as the thickness of the cell wall increases, as indicated in Fig. 23. This phenomenon could have been explained by the fact that as the thickness of the wall increases, the cell walls become more resistant to the bending and collapse of the cell. In order to produce

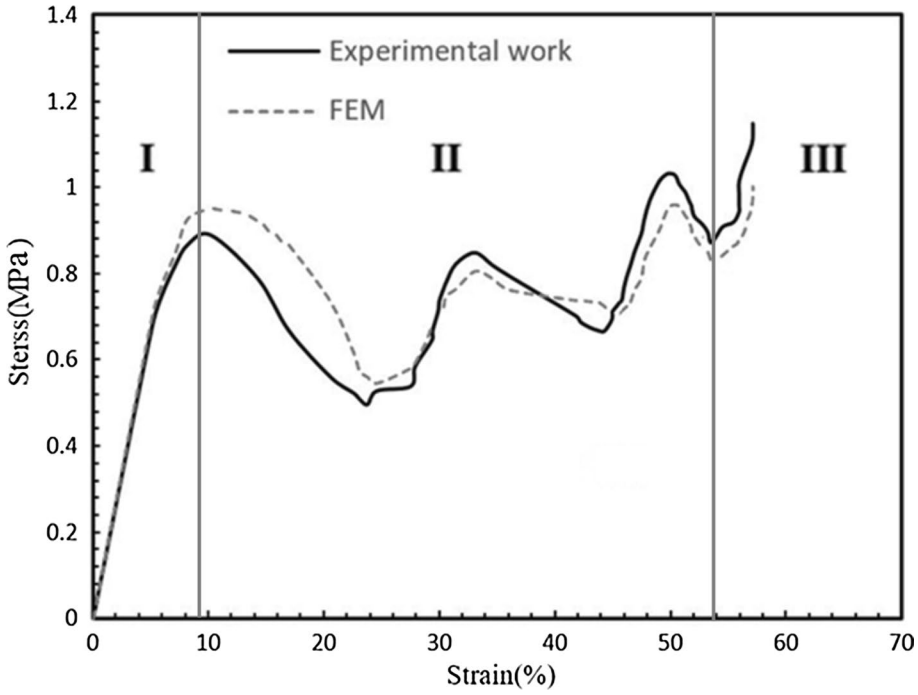

Fig. 12 Honeycomb structure stress–strain diagrams

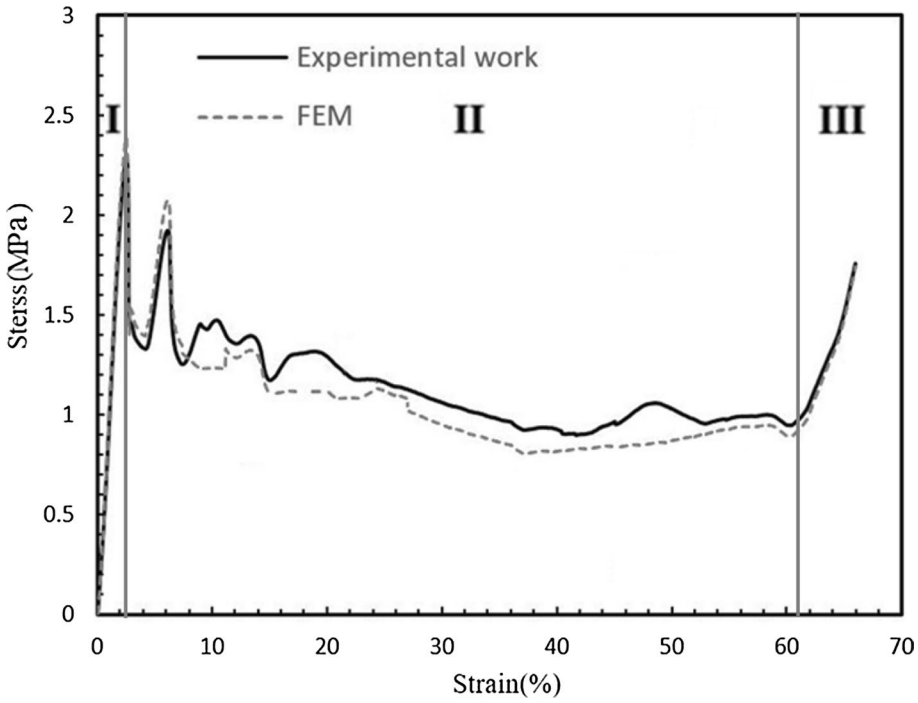

Fig. 13 Re-entrant auxetic structure stress–strain diagrams

displacement, more force is required because the cell walls collide sooner.

The amount of energy absorbed and specific energy absorbed for structures A1, t_1 and t_2, is shown in Table 5. The amount of energy absorbed and specific energy absorbed increases with increasing wall thickness.

Figures 25 and 26 show the stress–strain diagram and the Poisson's ratio in terms of strain concerning increments of L-parameter for structures A_0, l_1, andl_2, respectively. According to Fig. 27, with increasing value (L) increases, the density of the structure will decrease, so the amount of energy absorbed per unit volume will decrease; also, in Fig. 28, the maximum value of the negative Poisson's

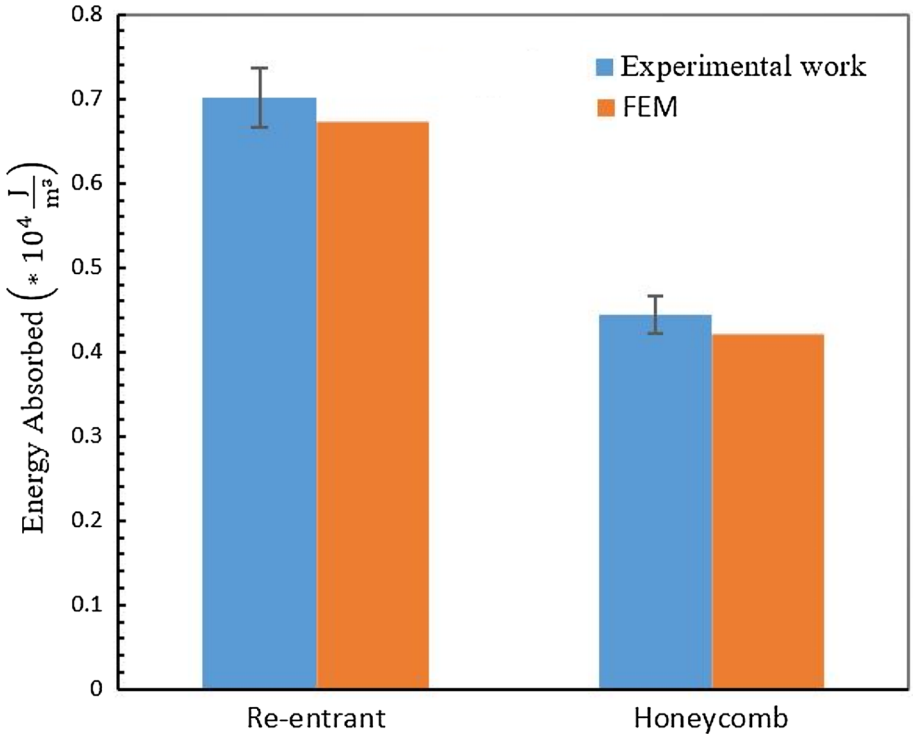

Fig. 14 Comparison diagram of the amount of energy absorption of structures

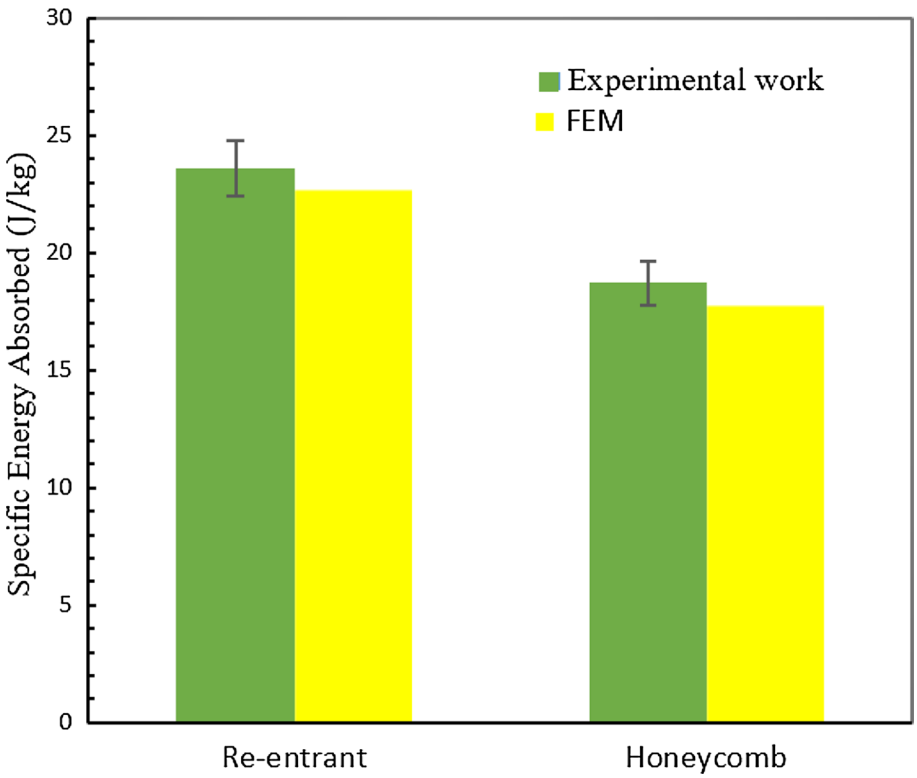

Fig. 15 Structures' specific energy absorption values

ratio is for the structure l_2 with a value of − 1.962. Table 5 shows the energy absorbed values.

Figures 27 and 28 show the stress–strain diagram and the Poisson's ratio diagram in terms of strain for three different values of the h-parameter (structures h_1, h_2, and A_0), respectively. Figure 29 demonstrates that by increasing the parameter h, the cross-sectional area to which the load is also applied increases; the amount of stress

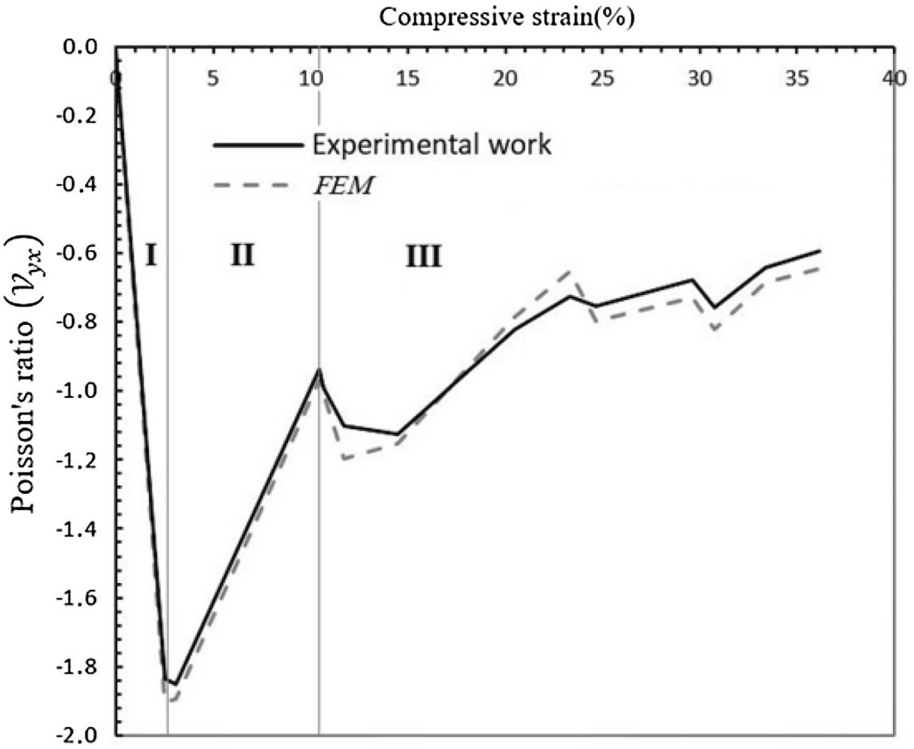

Fig. 16 NPR of the re-entrant auxetic structure

Table 2 Maximum NPR of the re-entrant auxetic structure

Compressive strain (%)	Poisson's ratio		
	Experiment	FEM	Error (%)
2.54	− 1.835	− 1.905	3.78

is thereby reduced; the amount of energy absorption decreases, as shown in Table 5. According to Fig. 30, as the parameter h increases, the NPR of the re-entrant auxetic structures decreases.

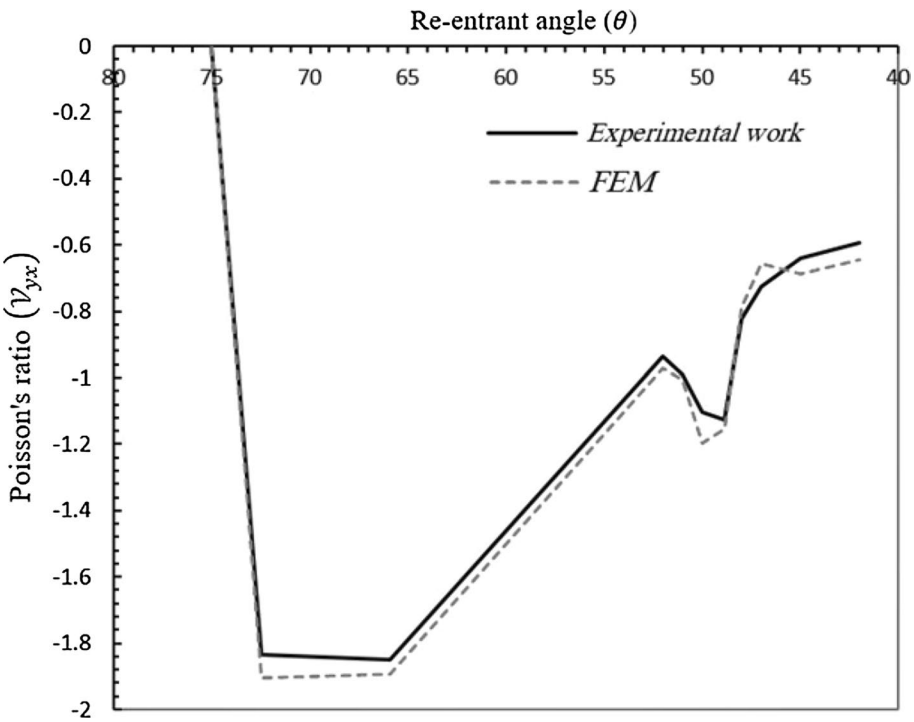

Fig. 17 Experimental and FEM of NPR for different re-entrant angles θ

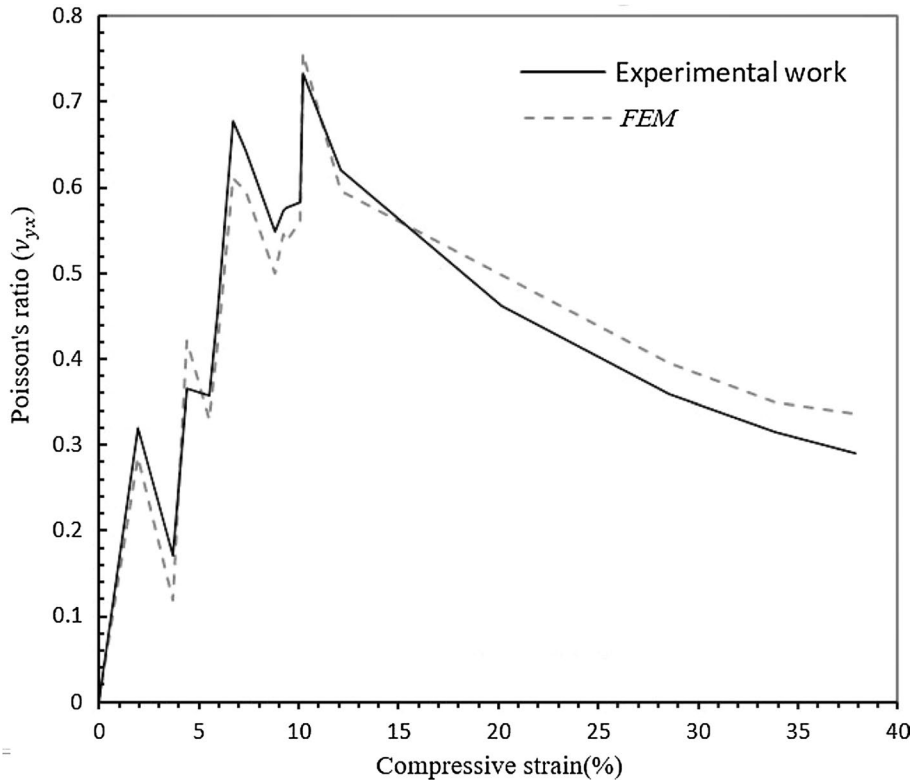

Fig. 18 Positive Poisson's ratio of the honeycomb structure

Table 3 Maximum Poisson's ratio of the honeycomb structure

Compressive strain (%)	Poisson's ratio		
	Experiment	FEM	Error%
10.18	0.734	0.757	3.19

Figure 29 shows the stress diagram in terms of strain for three different values of the initial angles of structures A_0, θ_1 and θ_2. According to Fig. 29, by reducing the initial angle from 75° to 65°, the energy absorption of the structure also increases, as shown in Table 5. As a result of reducing the inlet angle, due to the faster collision of the walls and the premature compaction of the structure, more force has to be applied to apply more strain. Also, by decreasing the initial angle, the maximum negative Poisson's ratio of the structure decreases, as shown in Fig. 30.

5 Conclusion

This study investigates and analyzes the compressive properties of re-entrant auxetic structures and non-auxetic honeycomb structures. To fabricate all models, additive manufacturing (3D printing) was used, and experimental results were compared with the results of finite element simulations. In uniaxial in-plane compressive loading, auxetic re-entrant structures demonstrated excellent performance in absorbing energy. The energy absorption and specific energy absorption rate of re-entrant auxetic structures were 57.75% and 26.19% more than non-auxetic honeycomb structures. This behavior of auxetic materials is similar to energy-absorbing materials; this expresses the extraordinary performance of auxetic structures in absorbing energy. Therefore, auxetic structures are an excellent alternative to energy absorbers and anti-impact protector structures. Also, in this study, the effective parameters of the structure geometry in the NPR of auxetic structures were investigated. It was observed that this behavior is highly dependent on the structure's geometry. In addition, considering the simulations performed on different materials, it was observed that the NPR behavior and the maximum negative Poisson's ratio of the structure are low sensitivity to structural materials. The results also show that the energy absorption of the structure with steel is 222.76% higher than PLA, and by choosing the material of the structure with more stiffness, the amount of energy absorption of the structure also increases.

Moreover, in this study, the effective geometrical parameters (θ, L, and h and t) on the Poisson's ratio were investigated, and it was observed that the Poisson's ratio decreases further as the two parameters (L and θ) increased in value. In other words, by increasing the above two parameters, Poisson's ratio became more negative, and the auxetic property increased. In contrast with these two parameters, Poisson's ratio rises with increasing

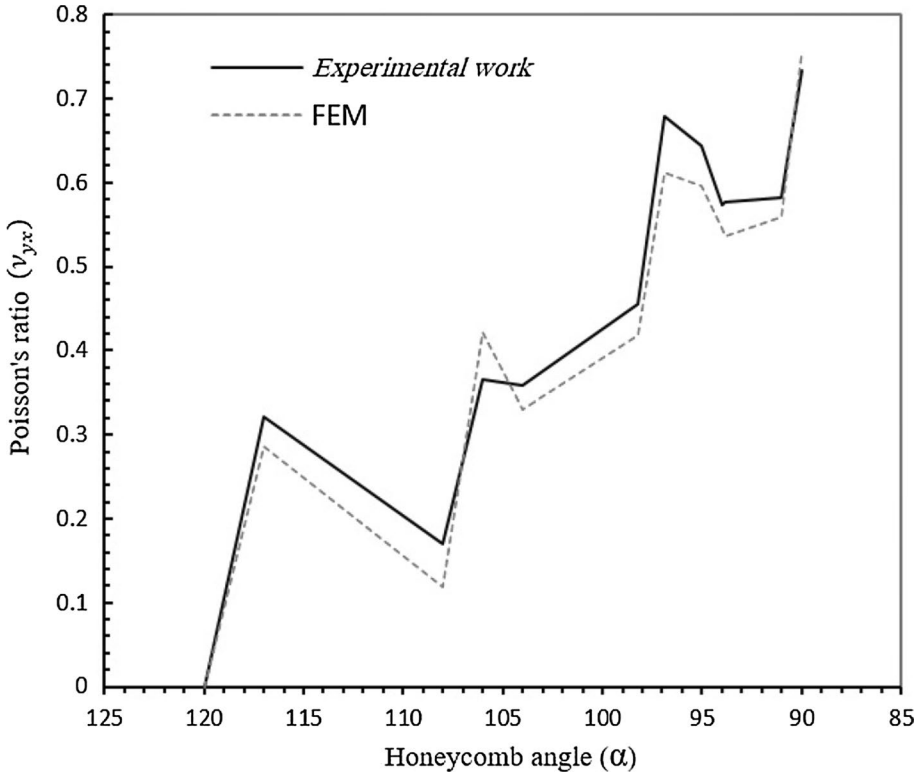

Fig. 19 FE simulation and experimental of the positive Poisson's ratio based on the angle $s(\alpha)$ of the honeycomb

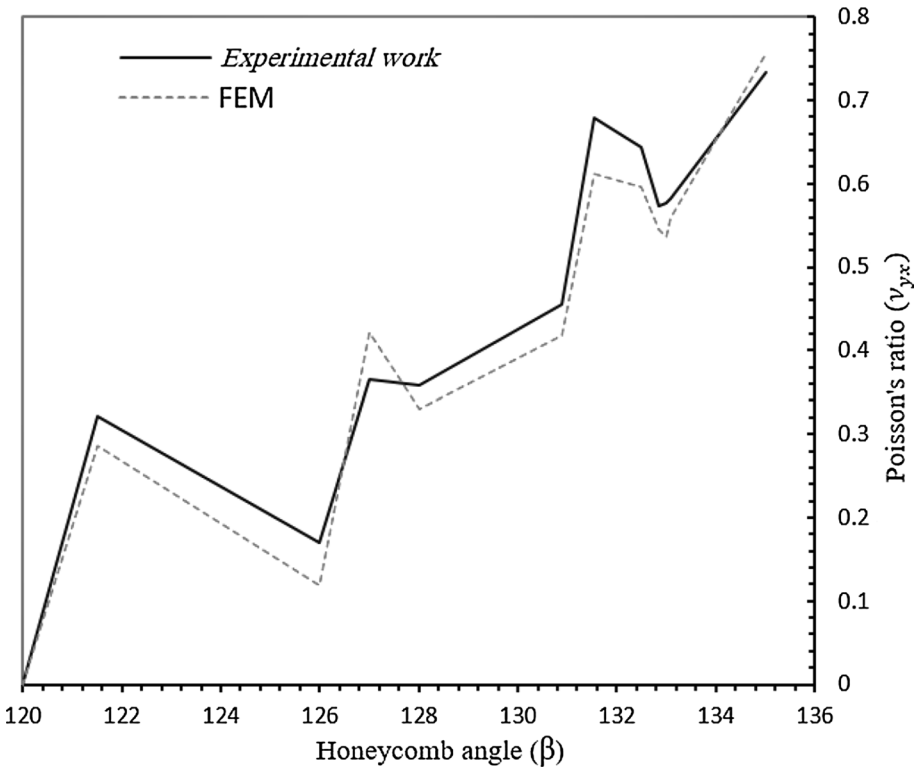

Fig. 20 FE simulation and experimental of the positive Poisson's ratio based on the angle $s(\beta)$ of the honeycomb

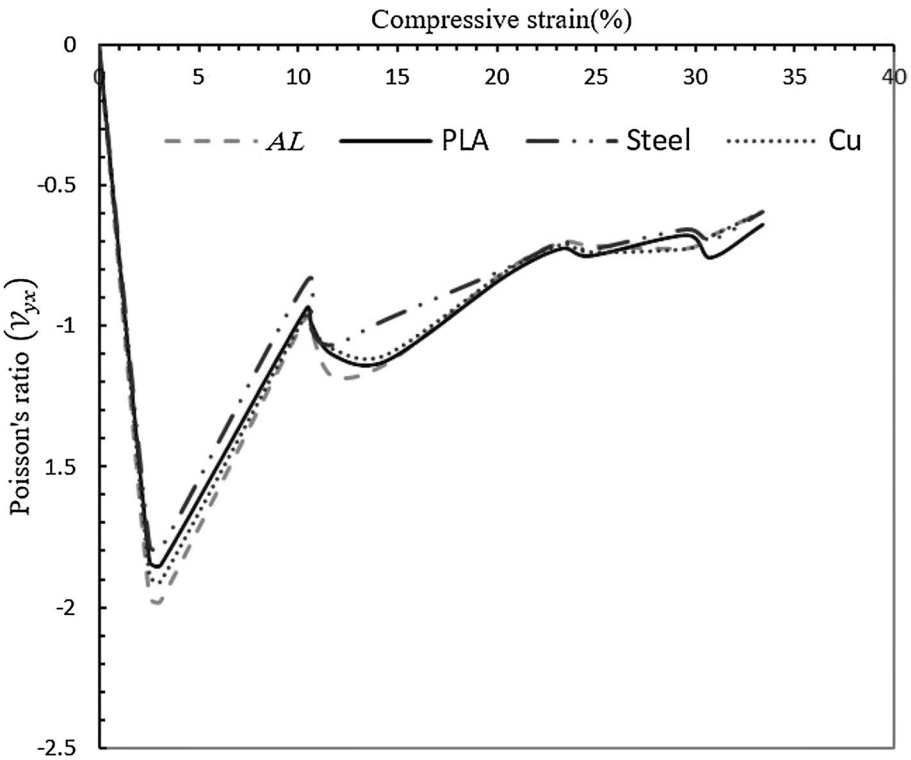

Fig. 21 NPR diagrams for different materials

Table 4 Maximum negative Poisson's ratio and energy adsorbed and specific energy absorbed for different materials used in the re-entrant auxetic structure

Material	ν_{max}	Energy Absorbed $\left(\frac{J}{m^2}\right)$	Specific Energy Absorbed $\left(\frac{J}{kg}\right)$
Al	-1.980	10,462.953	35.229
Cu	-1.906	11,481.581	38.658
PLA	-1.835	7015.353	23.621
Steel	-1.795	22,642.938	76.240

h and *t* (thickness), and the auxetic property decreased. In NPR behavior, the structure's geometry is more important than the material of the structure.

Also, in this research, the effect of geometric parameters on the amount of energy absorption, such as initial angle, wall thickness, and length of horizontal and oblique members through finite element simulation, was discussed.

The results related to the effect of geometric parameters show that by doubling the thickness of the structural walls, the energy absorption rate has increased by 818.80%, and by decreasing the initial angle from 75° to 65°, the energy absorption rate has increased by 43%; in addition, by increasing the length of the horizontal member (*h*) from 25.51 to 28 mm, the amount of energy absorbed decreased by 24.54%. As the mile (*l*) length increased from 12.375 to 14.864 mm, 19.78% of the energy absorbed decreased. The results show that increasing the thickness of the structure and decreasing the initial angle and length of the horizontal and oblique members increase the amount of energy absorption and specific energy absorbed. Due to the NPR behavior and energy absorption performance, these types of cellular structures can be used in various applications, such as crash absorbers and panels for impact and blast protection.

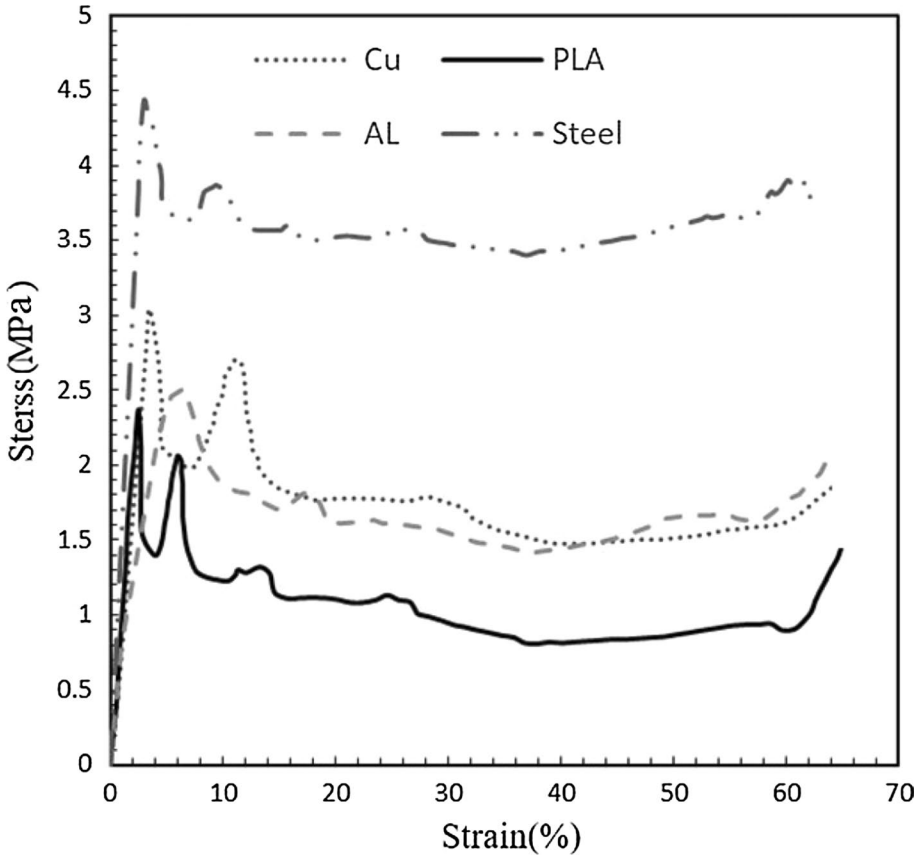

Fig. 22 Stress–strain diagrams for different materials

Table 5 Dimensions of each unit cell and comparison of energy absorption, specific energy absorbed, and the maximum negative Poisson's ratio of re-entrant auxetic structures with different geometric parameters

Structure	θ_0(Degree)	t(mm)	L(mm)	h(mm)	ν_{max}	Energy Absorbed $\left(\frac{J}{m^2}\right)$	Specific Energy Absorbed $\left(\frac{J}{kg}\right)$
A_0	75	2.25	12.375	25.51	-1.835	7015.353	23.621
t_1	75	3.375	12.375	25.51	-1.702	25,698.719	86.529
t_2	75	4.5	12.375	25.51	-1.433	64,457.463	217.031
l_1	73.22	2.25	13.375	25.51	-1.887	6556.267	22.075
l_2	70.64	2.25	14.864	25.51	-1.962	5627.5845	18.949
h_1	75	2.25	12.375	26.51	-1.818	6436.375	21.671
h_2	75	2.25	12.375	28	-1.741	5293.738	17.824
θ_1	70	2.25	12.375	25.51	-1.793	7668.820	25.823
θ_2	65	2.25	12.375	25.51	-1.687	10,031.955	33.778

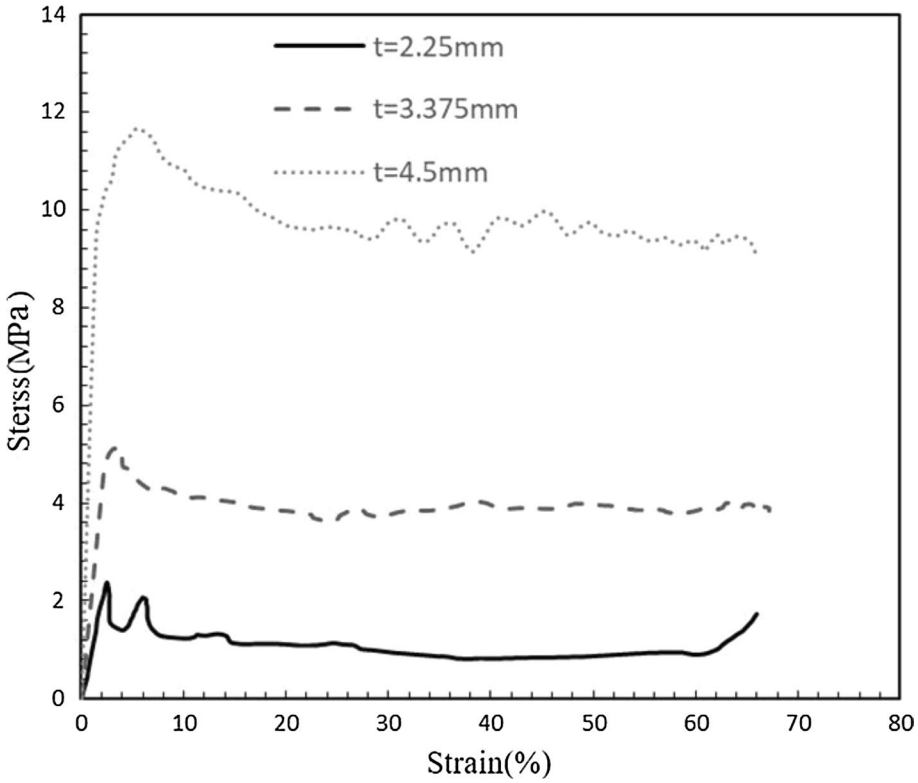

Fig. 23 Comparison of stress–strain diagram with the change of *t*-parameter

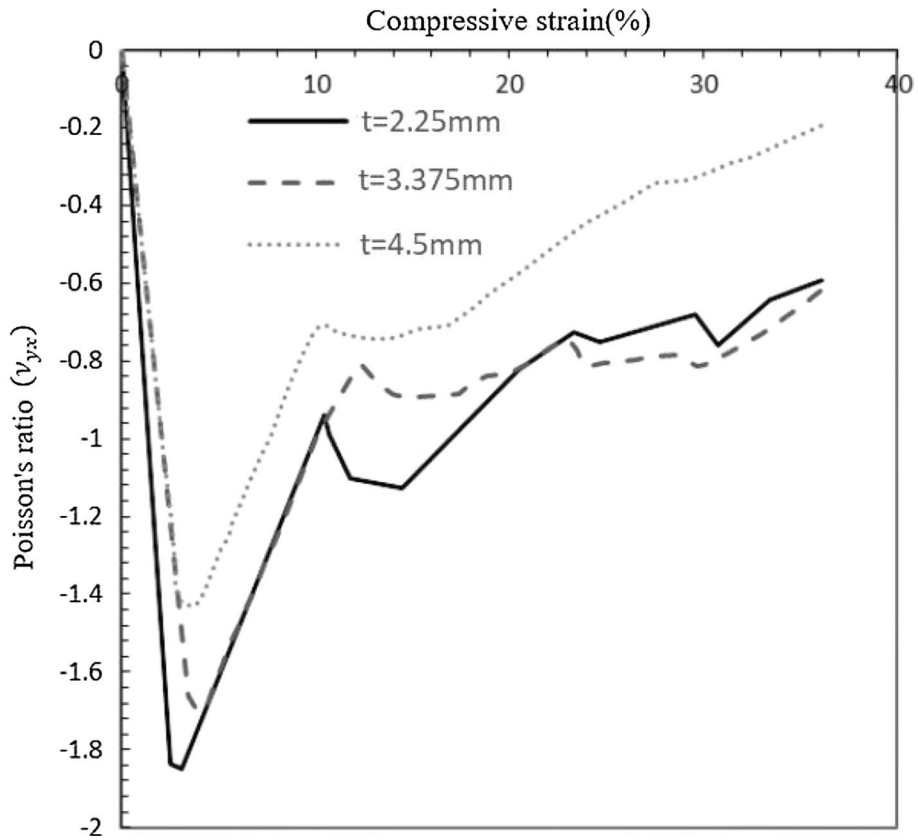

Fig. 24 Comparison of Poisson's ratio diagrams in terms of strain by changing the *t*-parameter

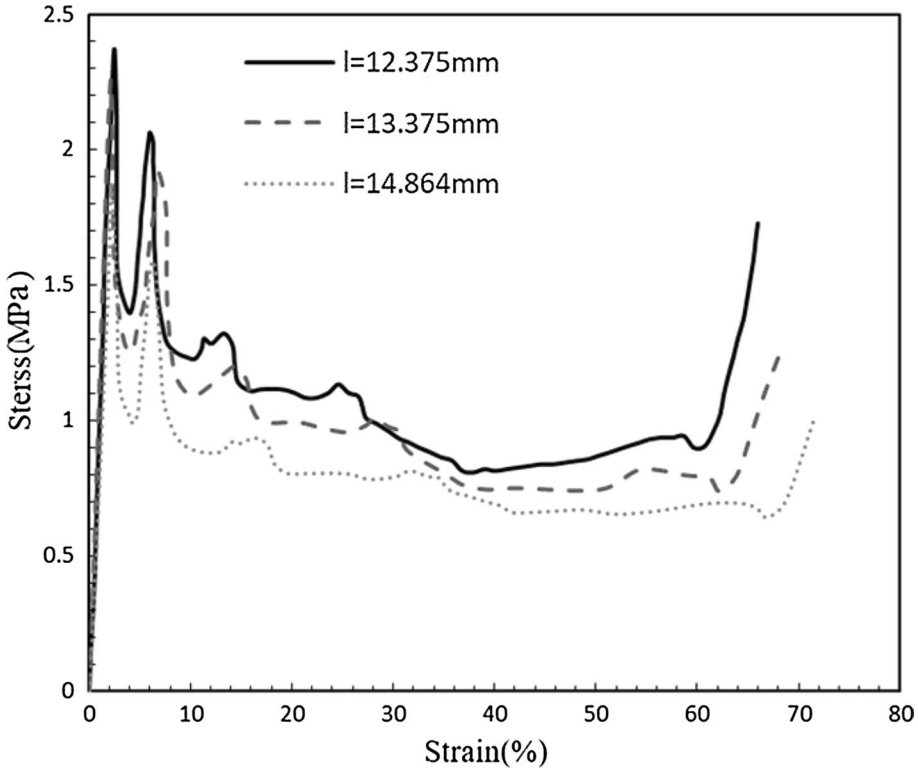

Fig. 25 Comparison of stress–strain diagram with the change of *l*-parameter

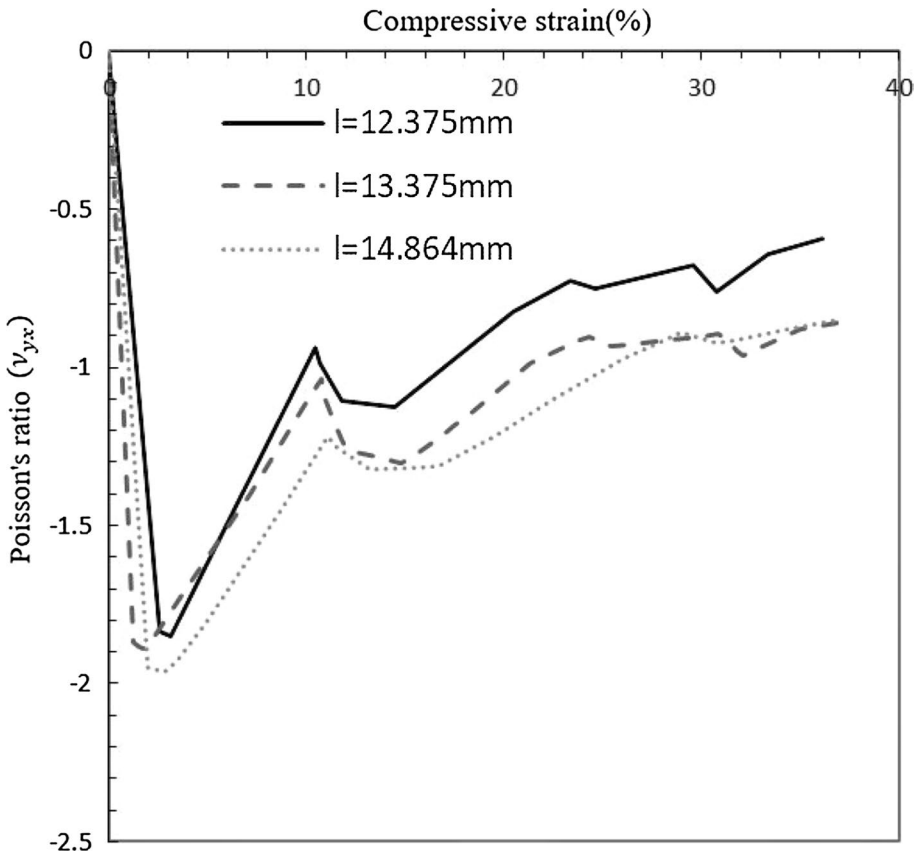

Fig. 26 Comparison of Poisson's ratio diagrams in terms of strain by changing the *l*-parameter

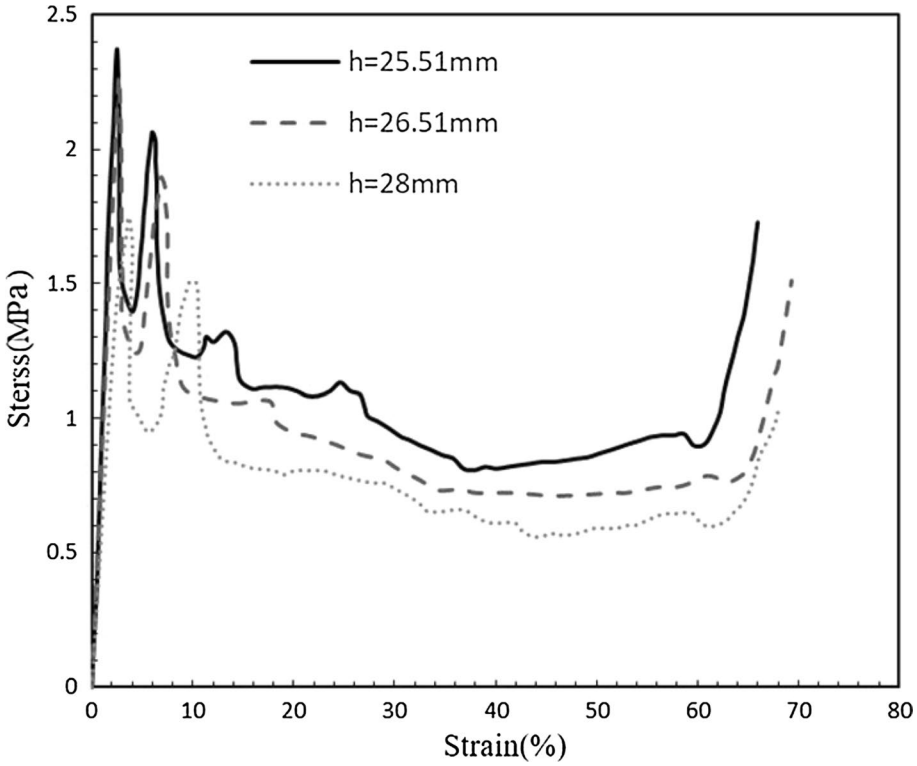

Fig. 27 Comparison of stress–strain diagram with the change of *h*-parameter

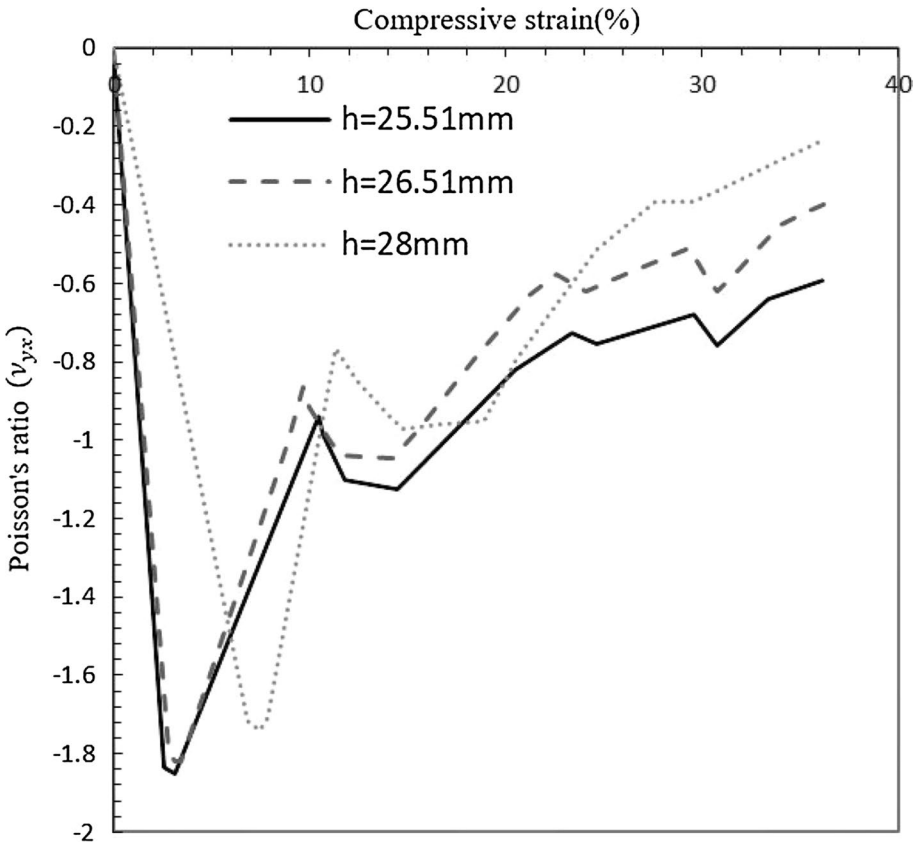

Fig. 28 Comparison of Poisson's ratio diagrams in terms of strain by changing the h-parameter

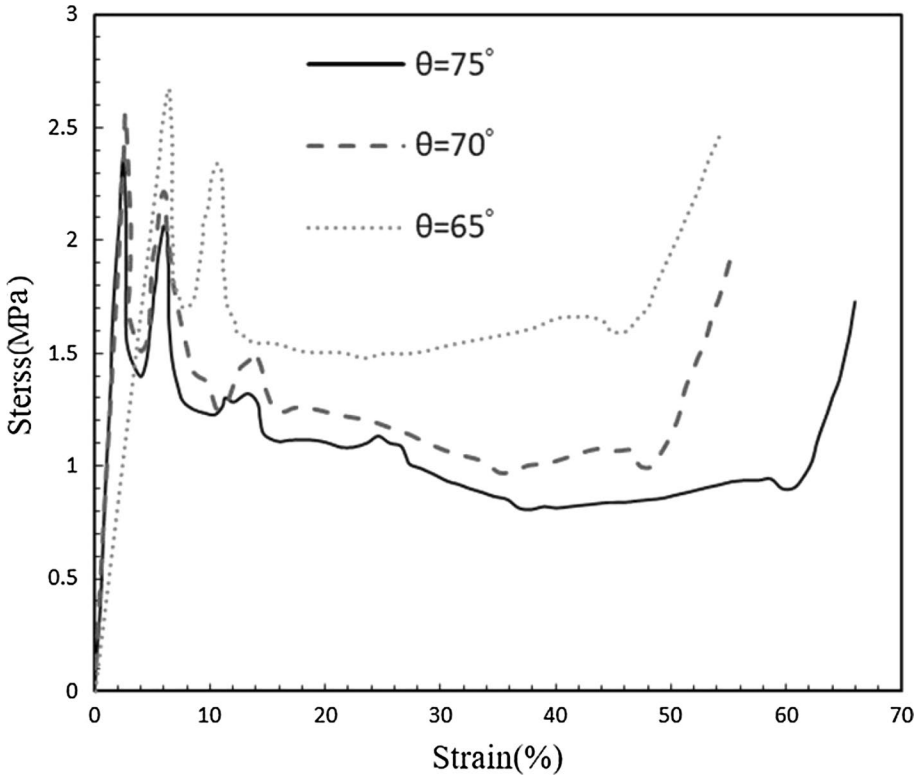

Fig. 29 Comparison of stress–strain diagram with the change of θ-parameter

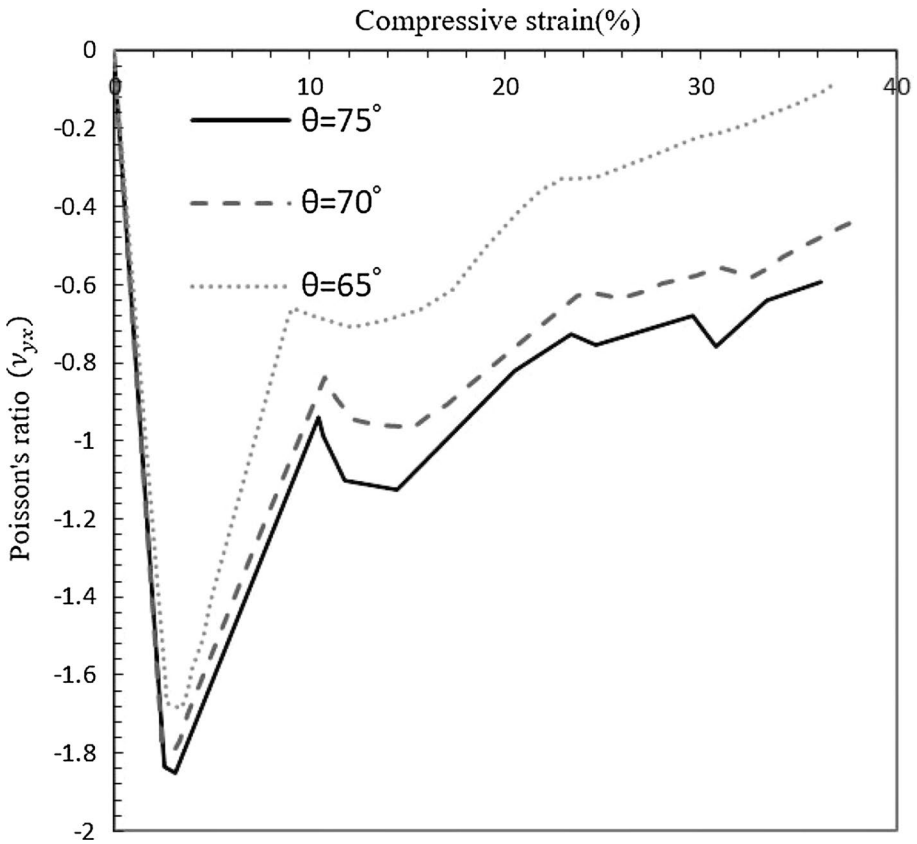

Fig. 30 Comparison of Poisson's ratio diagrams in terms of strain by changing the θ-parameter

Acknowledgements The authors would like to acknowledge Mr. Mehdi Emami-Moghadam for his assistance in samples construction and Mr. Akbar Mousavi for his contribution to conducting some of the experiments for the research in the Materials Department Laboratory of the Shahid Chamran University of Ahvaz. We are grateful to the Research Council of Shahid Chamran University of Ahvaz for financial support (GN1400/2/02/9281).

Data availability All the necessary data to reproduce the results reported here are provided in Sects. 2, 3, and 4. The data that support the findings of this study are available from the corresponding author upon reasonable request.

Declarations

Conflict of interest The authors declare no competing financial interest.

References

1. Voigt W (1893) Bestimmung der Elasticitätsconstanten für das chlorsaure Natron. Ann Phys 285:719–723. https://doi.org/10.1002/andp.18932850810
2. Evans K, Alderson A (2000) Auxetic materials: functional materials and structures from lateral thinking! Adv Mater 12:617–628. https://doi.org/10.1002/(SICI)1521-4095(200005)12:93.0.CO;2-3
3. Choi JB, Lakes RS (1992) Non-linear properties of polymer cellular materials with a negative Poisson's ratio. J Mater Sci 27:4678–4684. https://doi.org/10.1007/BF01166005
4. Alderson KL, Pickles AP, Neale PJ, Evans KE (1994) Auxetic polyethylene: the effect of a negative poisson's ratio on hardness. Acta Metall Mater 42:2261–2266. https://doi.org/10.1016/0956-7151(94)90304-2
5. Choi JB (1996) Fracture toughness of re-entrant foam materials with a negative Poisson's ratio: experiment and analysis. Int J Fract 80:73–83. https://doi.org/10.1007/BF00036481
6. Oh JH, Kim JS, Nguyen VH, Oh IK (2020) Auxetic graphene oxide-porous foam for acoustic wave and shock energy dissipation. Compos Part B Eng 186:107817. https://doi.org/10.1016/J.COMPOSITESB.2020.107817
7. Ma Z (2010) Towards a unified definition for reliability, survivability and resilience (I): the conceptual framework inspired by the handicap principle and ecological stability. In: IEEE Aerospace Confe Proc
8. Liu Q (2006) Literature review: materials with negative Poisson's ratios and potential applications to aerospace and defence
9. Parga Montemayor RD, Reyes Osorio LA, Lopez-Pavon L, et al (2022) Modeling of superelastic auxetic structures of Ti–Zr base alloy. Finite Elem Anal Des 201:103705. https://doi.org/10.1016/J.FINEL.2021.103705
10. Wang Z, Zulifqar A, Hu H (2016) Auxetic composites in aerospace engineering. Adv Compos Mater Aerosp Eng 213–240. https://doi.org/10.1016/B978-0-08-100037-3.00007-9
11. Peng R, Ma Y, He Z et al (2019) Single-layer Ag2S: a two-dimensional bidirectional auxetic semiconductor. Nano Lett. https://doi.org/10.1021/acs.nanolett.8b04761
12. Mardling P, Alderson A, Jordan-Mahy N, Le MCL (2020) The use of auxetic materials in tissue engineering. Biomater Sci 8:2074–2083. https://doi.org/10.1039/C9BM01928F
13. Duncan O, Foster L, Senior T, et al (2016) Quasi-static characterisation and impact testing of auxetic foam for sports safety applications. Smart Mater Struct 25:054014. https://doi.org/10.1088/0964-1726/25/5/054014
14. Duncan O, Shepherd T, Moroney C et al (2018) Review of auxetic materials for sports applications: expanding options in comfort and protection. Appl Sci 8:941. https://doi.org/10.3390/APP8060941
15. Jiang L, Gu B, Hu H (2016) Auxetic composite made with multilayer orthogonal structural reinforcement. Compos Struct 135:23–29. https://doi.org/10.1016/j.compstruct.2015.08.110
16. Jiang L, Hu H (2017) Low-velocity impact response of multilayer orthogonal structural composite with auxetic effect. Compos Struct 169:62–68. https://doi.org/10.1016/j.compstruct.2016.10.018
17. Nasim MS, Etemadi E (2017) Analysis of effective parameters of auxetic composite structure made with multilayer orthogonal reinforcement by finite element method. Modares Mech Eng
18. Safikhani Nasim M, Etemadi E (2018) Three dimensional modeling of warp and woof periodic auxetic cellular structure. Int J Mech Sci 136:475–481. https://doi.org/10.1016/j.ijmecsci.2018.01.002
19. Hu H, Silberschmidt V (2013) A composite material with Poisson's ratio tunable from positive to negative values: an experimental and numerical study. J Mater Sci 48:8493–8500. https://doi.org/10.1007/s10853-013-7666-1
20. Fu MH, Chen Y, Hu LL (2017) A novel auxetic honeycomb with enhanced in-plane stiffness and buckling strength. Compos Struct 160:574–585. https://doi.org/10.1016/J.COMPSTRUCT.2016.10.090
21. Mizzi L, Attard D, Gatt R et al (2015) Influence of translational disorder on the mechanical properties of hexachiral honeycomb systems. Compos Part B Eng 80:84–91. https://doi.org/10.1016/J.COMPOSITESB.2015.04.057
22. Wang ZP, Poh LH, Zhu Y, et al (2019) Systematic design of tetra-petals auxetic structures with stiffness constraint. Mater Des 170:107669. https://doi.org/10.1016/J.MATDES.2019.107669
23. Jin X, Wang Z, Ning J et al (2016) Dynamic response of sandwich structures with graded auxetic honeycomb cores under blast loading. Compos Part B Eng 106:206–217. https://doi.org/10.1016/J.COMPOSITESB.2016.09.037
24. Wang T, Wang L, Ma Z, Hulbert GM (2018) Elastic analysis of auxetic cellular structure consisting of re-entrant hexagonal cells using a strain-based expansion homogenization method. Mater Des 160:284–293. https://doi.org/10.1016/J.MATDES.2018.09.013
25. Gao Q, Wang L, Zhou Z et al (2018) Theoretical, numerical and experimental analysis of three-dimensional double-V honeycomb. Mater Des 139:380–391. https://doi.org/10.1016/J.MATDES.2017.11.024
26. Hu LL, Yu TX (2010) Dynamic crushing strength of hexagonal honeycombs. Int J Impact Eng 37:467–474. https://doi.org/10.1016/J.IJIMPENG.2009.12.001
27. Qi C, Remennikov A, Pei LZ et al (2017) Impact and close-in blast response of auxetic honeycomb-cored sandwich panels: experimental tests and numerical simulations. Compos Struct 180:161–178. https://doi.org/10.1016/J.COMPSTRUCT.2017.08.020
28. Hu LL, Wu ZJ, Fu MH (2018) Mechanical behavior of anti-trichiral honeycombs under lateral crushing. Int J Mech Sci 140:537–546. https://doi.org/10.1016/J.IJMECSCI.2018.03.039
29. Qi C, Yang S, Wang D, Yang LJ (2013) Ballistic resistance of honeycomb sandwich panels under in-plane high-velocity impact. Sci World J 2013:. https://doi.org/10.1155/2013/892781
30. Grujicic M, Yavari R, Snipes JS, Ramaswami S (2015) A zeolite absorbent/nano-fluidics protection-based blast- and ballistic-impact-mitigation system. J Mater Sci 50:2019–2037. https://doi.org/10.1007/s10853-014-8779-x

31. Wang XT, Li XW, Ma L (2016) Interlocking assembled 3D auxetic cellular structures. Mater Des 99:467–476. https://doi.org/10.1016/j.matdes.2016.03.088
32. Bates SRG, Farrow IR, Trask RS (2016) 3D printed polyurethane honeycombs for repeated tailored energy absorption. Mater Des 112:172–183. https://doi.org/10.1016/j.matdes.2016.08.062
33. Yuan S, Shen F, Bai J et al (2017) 3D soft auxetic lattice structures fabricated by selective laser sintering: TPU powder evaluation and process optimization. Mater Des 120:317–327. https://doi.org/10.1016/j.matdes.2017.01.098
34. Evans KE (1991) The design of doubly curved sandwich panels with honeycomb cores. Compos Struct 17:95–111. https://doi.org/10.1016/0263-8223(91)90064-6
35. Yang C, Vora HD, Chang Y (2018) Behavior of auxetic structures under compression and impact forces. Smart Mater Struct 27:025012. https://doi.org/10.1088/1361-665X/aaa3cf
36. Hamzehei R, Kadkhodapour J, Anaraki AP et al (2018) Octagonal auxetic metamaterials with hyperelastic properties for large compressive deformation. Int J Mech Sci 145:96–105. https://doi.org/10.1016/j.ijmecsci.2018.06.040
37. Zhang XC, Ding HM, An LQ, Wang XL (2015) Numerical investigation on dynamic crushing behavior of auxetic honeycombs with various cell-wall angles. Adv Mech Eng. https://doi.org/10.1155/2014/679678
38. Ingrole A, Hao A, Liang R (2017) Design and modeling of auxetic and hybrid honeycomb structures for in-plane property enhancement. Mater Des 117:72–83. https://doi.org/10.1016/j.matdes.2016.12.067
39. Ren X, Das R, Tran P, et al (2018) Auxetic metamaterials and structures: a review. Smart Mater Struct 27
40. Xu W, Ma P, Wu L, Jiang G (2020) Low-velocity impact properties of composite reinforced by auxetic warp-knitted spacer fabric. https://doi.org/10.1177/1099636220908569
41. Qi C, Jiang F, Remennikov A, et al (2020) Quasi-static crushing behavior of novel re-entrant circular auxetic honeycombs. Compos Part B Eng 197:108117. https://doi.org/10.1016/J.COMPOSITESB.2020.108117
42. Meena K, Singamneni S (2019) A new auxetic structure with significantly reduced stress concentration effects. Mater Des 173:107779. https://doi.org/10.1016/J.MATDES.2019.107779
43. Hur JM, Seo DS, Kim K, et al (2021) Harnessing distinct deformation modes of auxetic patterns for stiffness design of tubular structures. Mater Des 198:109376. https://doi.org/10.1016/J.MATDES.2020.109376
44. Mizzi L, Salvati E, Spaggiari A, et al (2020) Highly stretchable two-dimensional auxetic metamaterial sheets fabricated via direct-laser cutting. Int J Mech Sci 167:105242. https://doi.org/10.1016/J.IJMECSCI.2019.105242
45. Linforth S, Ngo T, Tran P, et al (2021) Investigation of the auxetic oval structure for energy absorption through quasi-static and dynamic experiments. Int J Impact Eng 147:103741. https://doi.org/10.1016/J.IJIMPENG.2020.103741
46. Ajdari A, Jahromi BH, Papadopoulos J et al (2012) Hierarchical honeycombs with tailorable properties. Int J Solids Struct 49:1413–1419. https://doi.org/10.1016/J.IJSOLSTR.2012.02.029
47. Choi JB, Lakes RS (1995) Analysis of elastic modulus of conventional foams and of re-entrant foam materials with a negative Poisson's ratio. Int J Mech Sci 37:51–59. https://doi.org/10.1016/0020-7403(94)00047-N
48. Zhang ZK, Hu H, Xu BG (2013) An elastic analysis of a honeycomb structure with negative Poisson's ratio. Smart Mater Struct 22:084006. https://doi.org/10.1088/0964-1726/22/8/084006
49. Imbalzano G, Linforth S, Ngo TD et al (2018) Blast resistance of auxetic and honeycomb sandwich panels: Comparisons and parametric designs. Compos Struct 183:242–261. https://doi.org/10.1016/J.COMPSTRUCT.2017.03.018
50. Etemadi E, Zamani J, Francesconi A et al (2014) A new setup to investigate plastic deformation of face centered cubic metals in high strain rate loading. Mod Appl Sci 8:94–106. https://doi.org/10.5539/MAS.V8N2P94
51. Safikhani Nasim M, Etemadi E (2018) Three dimensional modeling of warp and woof periodic auxetic cellular structure. Int J Mech Sci 136:. https://doi.org/10.1016/j.ijmecsci.2018.01.002
52. Etemadi E, Molla-Mohammad Zamani AR, Safikhani-Nasim M (2021) Experimental and numerical analysis of effective geometrical parameters for energy absorbing of the structures with negative Poisson's ratio made from aluminium alloy 1100. J Solid Fluid Mech 11:311–324
53. Becker R, Vexler B (2005) Mesh refinement and numerical sensitivity analysis for parameter calibration of partial differential equations. J Comput Phys 206:95–110. https://doi.org/10.1016/j.jcp.2004.12.018
54. Aborehab A, Kassem M, Nemnem AF, Kamel M (2020) Miscellaneous modeling approaches and testing of a satellite honeycomb sandwich plate. J Appl Comput Mech 6:1084–1097. https://doi.org/10.22055/JACM.2019.31255.1846
55. Schoonjans F (2012) Digimizer manual: easy-to-use image analysis software. 107
56. Tarigopula V, Langseth M, Hopperstad OS, Clausen AH (2006) Axial crushing of thin-walled high-strength steel sections. Int J Impact Eng, pp 847–882
57. Meguid SA, Stranart JC, Heyerman J (2004) On the layered micromechanical three-dimensional finite element modelling of foam-filled columns. Finite Elem Anal Des 40:1035–1057. https://doi.org/10.1016/j.finel.2002.02.001
58. Santosa SP, Wierzbicki T, Hanssen AG, Langseth M (2000) Experimental and numerical studies of foam-filled sections. Int J Impact Eng 24:509–534. https://doi.org/10.1016/S0734-743X(99)00036-6
59. Aktay L, Toksoy AK, Güden M (2006) Quasi-static axial crushing of extruded polystyrene foam-filled thin-walled aluminum tubes: experimental and numerical analysis. Mater Des 27:556–565. https://doi.org/10.1016/j.matdes.2004.12.019
60. Gibson LJ, Ashby MF (1999) Cellular solids structure and properties
61. Bitzer T (1997) Introduction. Honeycomb Technol 1–9. https://doi.org/10.1007/978-94-011-5856-5_1